J. Fluid Mech. (2025), *vol.* 1020, A3, doi:10.1017/jfm.2025.10657

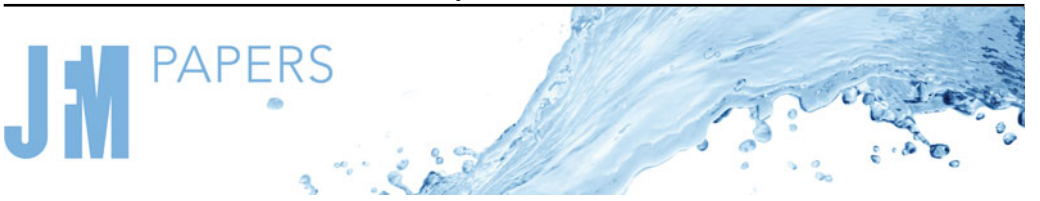

Destabilisation of leading-edge shear layer behind wall-mounted long prisms

Shubham Goswami[1] **and Arman Hemmati**[1]

[1]Department of Mechanical Engineering, University of Alberta, Edmonton, AB T6G 2R3, Canada

Corresponding author: Arman Hemmati, arman.hemmati@ualberta.ca

(Received 18 December 2024; revised 19 July 2025; accepted 1 September 2025)

This numerical investigation focuses on the mechanisms, flow topology and onset of Kelvin–Helmholtz instabilities (KHIs), that drive the leading-edge shear-layer destabilisation in the wake of wall-mounted long prisms. Large-eddy simulations are performed at $Re = 2.5 \times 10^3$, 5×10^3 and 1×10^4 for prisms with a range of aspect ratio (AR, height-to-width) between 0.25 and 1.5, and depth ratios (DR, length-to-width) of $1-4$. Results show that shear-layer instabilities enhance flow irregularity and modulate spanwise vortex structures. The onset of KHI is strongly influenced by depth ratio, such that long prisms ($DR = 4$) experience earlier initiation compared with shorter ones ($DR = 1$). At higher Reynolds numbers, the onset of KHI shifts upstream towards the leading-edge, intensifying turbulence kinetic energy and increasing flow irregularity, especially for long prisms. The results further show that in this configuration, energy transfer from the secondary recirculation region contributes to the destabilisation of the leading-edge shear layer by reinforcing low-frequency modes. A feedback mechanism is identified wherein energetic flow structures propagate upstream through reverse boundary-layer flow, re-energising the leading-edge shear layer. Quantification using probability density functions reveals rare, intense upstream energy convection events, driven by this feedback mechanism. These facilitate the destabilisation process regardless of Reynolds number. This study provides a comprehensive understanding of the destabilisation mechanisms for leading-edge shear layers in the wake of wall-mounted long prisms.

Key words: wakes, separated flows, vortex dynamics

1. Introduction

The analysis of unsteady flow past wall-mounted bluff bodies is of significant practical importance due to its relevance across a broad range of engineering applications. At high

Reynolds numbers, such flows are encountered in the aerodynamics of high-rise buildings (Tominaga 2015), chimneys (Jiang & Yoshie 2020), tube banks in heat exchangers (Mangrulkar *et al.* 2017), and in the wakes of trains and trucks (Paul, Johnson & Yates 2009). These configurations often give rise to complex flow phenomena, including flow separation, recirculation, shear-layer instabilities and large-scale vortex shedding, which can lead to unsteady loading, acoustic noise and vortex-induced vibrations. At low Reynolds numbers, similar bluff-body flow behaviour is observed in microfluidic systems and electronics cooling applications (Rastan, Sohankar & Alam 2017), as well as in physiological flows over wall roughness in arteries (Jia *et al.* 2021) and engineered roughness elements in internal pipe flows (Goswami & Hemmati 2020, 2021*a*,*b*).

Dynamics of flow separation due to abrupt changes in surface conditions, such as the presence of an obstacle, is particularly important in studies related to the flow over prisms. Turbulent flow around wall-mounted prisms, or step change in the flow, presents a class of perturbed or non-equilibrium flow, the behaviour of which is typically complex (Wang & Zhou 2009; Smits *et al.* 2019; Goswami & Hemmati 2020, 2021*a*). Abrupt surface variations, especially in the presence of a prism, create a contraction in the flow, which leads to an overshoot in flow characteristics, such as the formation of larger pressure gradients and higher Reynolds shear stresses, in the vicinity of the prism. It also results in the formation and interactions of various flow structures in the wake. Moreover, flow past wall-mounted prisms constitutes a classical problem in fluid mechanics. In contrast to aerodynamic bodies at low angles of attack, sharp-edged bodies have an extended flow region of velocity deficit behind them, referred to as the wake (Von Kármán 1963). Topology or organisation of the wake is dictated by both the transient and time-averaged (mean) nature of the vortex formations and their interactions. The wake of wall-mounted prisms is typically complex and highly three-dimensional due to various end-effects, including the free-end and junction flows (Wang & Zhou 2009). The flow response to wall-mounted obstacles have thus motivated extended research in the field of separated flow, such as flow over wall-mounted prisms (Martinuzzi & Tropea 1993; Hussein & Martinuzzi 1996; Wang & Lam 2019; Goswami & Hemmati 2022, 2023, 2024; Goswami 2025; Shojaee *et al.* 2025) and internal flow over prisms (Yakhot, Liu & Nikitin 2006; Smits *et al.* 2019; Goswami & Hemmati 2020, 2021*b*).

Vortical structures in the wake of wall-mounted prisms are significantly affected by flow parameters, such as Reynolds number (Hwang & Yang 2004; Zhang *et al.* 2017), boundary layer thickness (Hosseini, Bourgeois & Martinuzzi 2013; El Hassan, Bourgeois & Martinuzzi 2015) and geometrical parameters, including aspect ratio *(AR*, height-to-width*)* (Wang *et al.* 2006; Wang & Zhou 2009; Saha 2013), incident (yaw) angle (Becker, Lienhart & Durst 2002), cross-sectional shape (Uffinger, Ali & Becker 2013; Kindree, Shahroodi & Martinuzzi 2018) and depth ratio (*DR*, length-to-width) (Rastan *et al.* 2021; Goswami & Hemmati 2024). An abundance of literature exists that focus on the effects of aspect ratio (Sakamoto & Arie 1983; Wang & Zhou 2009; Saha 2013) and Reynolds number (Wang & Lam 2019; Yauwenas *et al.* 2019) on characterising large-scale vortical structures behind wall-mounted finite prisms. Despite these efforts, there has not been a comprehensive study of the cylinder depth ratio on wake mechanisms and vortex development.

Rastan *et al.* (2021) was the first to highlight the impact of depth ratio on the flow topology and vortex shedding characteristics. They observed that depth ratio significantly affects flow irregularity and vortex shedding, where the wake of long prisms ($DR \geqslant 2$) exhibit highly three-dimensional structures and enhanced vortex shedding compared with short prisms ($DR = 1$). Similarly, Zargar, Tarokh & Hemmati (2022) examined the onset of flow irregularity and unsteady wake behind small aspect ratio, wall-mounted

long prisms at $Re \geqslant 750$. Their findings linked the onset of irregular unsteady wake to destabilisation of the leading-edge shear-layer, which initiates the formation of hairpin-like vortices. Despite these advances, the precise mechanism underlying the leading-edge shear-layer destabilisation remains unclear. Moreover, the influence of depth ratio on the destabilisation mechanism and subsequent wake irregularity has not been thoroughly investigated. Further, these mechanisms are not well understood for wall-mounted prisms, where the flow topology is significantly different from suspended prisms.

Leading-edge shear-layer separation and reattachment is a defining feature of the flow around wall-mounted prisms (Rastan *et al.* 2021; Goswami & Hemmati 2024, 2025). This flow combines small-scale phenomenon, resulting from the turbulent motions near the leading edge, with the large-scale vortex shedding. These scales interact nonlinearly, amplifying wake irregularity and causing significant variations in surface pressure distributions (Goswami & Hemmati 2024). However, a complete understanding of these interacting processes and their impact on flow topology is not yet achieved. A key factor in destabilisation of the leading-edge shear layer is the interaction between large-scale vortex shedding and small-scale turbulent motions in the wake (Goswami & Hemmati 2024). As suggested by Goswami & Hemmati (2025), this interaction is further modulated by depth ratio, which governs the extent of flow separation and reattachment on the prism surfaces.

Destabilisation of the leading-edge shear layer, and subsequent formation of hairpin-like vortices, was previously observed in the flow around suspended prisms (Cimarelli, Leonforte & Angeli 2018; Kumahor & Tachie 2022), where the leading-edge shear layer undergoes a series of instabilities, leading to the formation of hairpin-like vortices. Two major instabilities were identified, including the primary Kelvin–Helmholtz instability (KHI) of the leading-edge shear layer and instability of the primary recirculation bubble (Sigurdson 1995). Kelvin–Helmholtz instability is characterised by shedding of a pseudo-periodic train of co-rotating vortical structures from the leading-edge shear layer (Kiya & Sasaki 1983). Additionally, Kiya & Sasaki (1983) observed low-frequency shear-layer flapping, accompanied by enlargement and shrinkage of the primary recirculation bubble. In terms of flow topology, these mechanisms exhibit well-defined vortical motions. For example, KHI produces spanwise vortex rollers that undergo secondary instabilities, forming hairpin-like vortices (Zhang *et al.* 2023). Similarly, instability of the primary recirculation bubble forms streamwise vortex tubes, which entrain high- and low-speed fluid, leading to large-scale vortex shedding in the wake (Jimenez 1983). Further complexities arise from the induced reattachment of the leading-edge shear layer on prism surfaces and formation of secondary recirculation regions. These secondary recirculation regions feature reverse flow and an upstream-moving boundary layer, leading to a feedback mechanism identified by Cimarelli *et al.* (2018). While the flow topology around suspended prisms is relatively well understood, that of wall-mounted prisms remains unexplored in the literature.

This study investigates destabilisation mechanisms of the leading-edge shear layer in the wake of wall-mounted long prisms with varying depth ratios. The focus is on the onset of KHI, which amplifies flow irregularity and modulates spanwise vortex structures, contributing to the destabilisation process. Numerical simulations are performed in this study at Reynolds numbers of $Re = 2.5 \times 10^3 - 1 \times 10^4$ for wall-mounted prisms with aspect ratios of $0.25-1.5$ and a range of depth ratios $(1-4)$. For brevity, we focus our main analysis on the case of $Re = 2.5 \times 10^3$, $AR = 1$, and $DR = 1$ and 4, which represent the short and long prisms, respectively. All our findings and arguments, however, remain valid for the entire parameter space. This article is structured as follows: § 2 describes the problem setup and validation of the numerical simulations; § 3 presents the results and

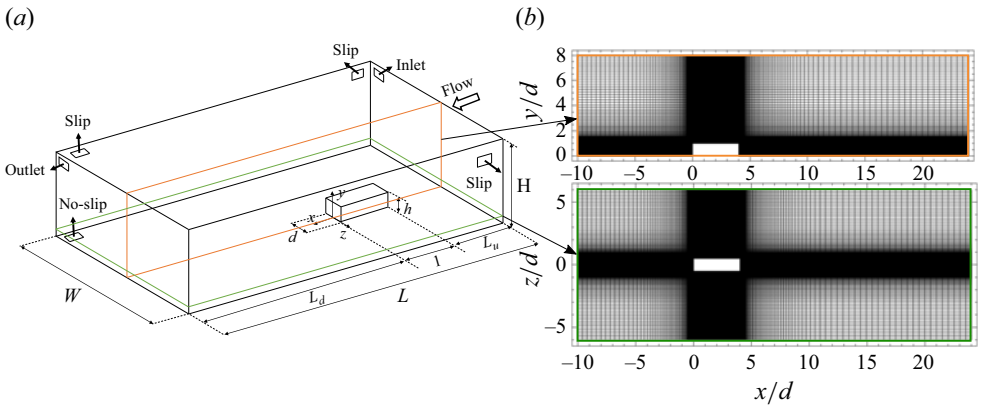

Figure 1. (*a*) Computational domain (not to scale) and (*b*) spatial grid distribution for the wall mounted thin prism of $DR = 4$, presented in top view at $y/d = 0.5$ (top) and side view at $z/d = 0$ (bottom).

discussion, focusing on the destabilisation of the leading-edge shear layer and formation of hairpin-like vortices; and the conclusions are presented in § 4.

2. Problem description

Large-eddy simulation (LES) with the dynamic Smagorinsky sub-grid scale model (Durbin & Reif 2011) was used to investigate the wake in OpenFOAM. The computational domain consisted of a rectangular prism with aspect ratios ($AR = h/d$) of 0.25, 0.5, 1 and 1.5, and depth ratios ($DR = l/d$) of 1, 2, 3 and 4 mounted on the base of the domain with dimensions $L_u = 10d$, $L_d = 20d$, $H = 6d{-}8d$ and $W = 12d$, where the domain height was adjusted to account for the larger aspect-ratio prisms. Numerical simulations were performed at Reynolds numbers of $Re = U_b d/\nu = 2.5 \times 10^3 {-} 1 \times 10^4$, with increments of 2.5×10^3, where U_b is the bulk velocity, d is the width of the prism and ν is the kinematic viscosity. The study employed a non-homogeneous structured grid comprising 25×10^6 and 76×10^6 elements, depending on the depth ratio (DR) and Reynolds number. The domain and grid for $DR = 4$ are presented in figure 1. The inlet boundary condition was set to uniform flow ($u = U_b$, $v = w = 0$), with an outflow boundary condition ($\partial u/\partial n = \partial p/\partial n = 0$) applied at the outlet. Ceiling and lateral boundaries were modelled as free-slip, while no-slip wall condition was imposed on the ground and the prism. This computational set-up closely resembled those of Goswami & Hemmati (2022) and Goswami & Hemmati (2025). The natural boundary layer thickness (δ) varied between $\delta/d \approx 1.2$ and 0.8 for $Re = 2.5 \times 10^3$ and 1×10^4, respectively, when simulating the flow without placing the prism in the domain. Boundary layer thickness was determined as the distance from the wall to the location where the streamwise mean velocity reaches 99 % of the free stream velocity. Moreover, the prism was fully immersed in the boundary layer. As an example, the boundary layer thickness at $Re = 2.5 \times 10^3$ was $\delta/d \approx 1.2$ as shown in figure 2. Since the boundary layer thickness changed with Reynolds number, the influence of boundary layer thickness on the wake topology was incorporated in the current analysis. As noted by Behera & Saha (2019), the implications of boundary layer thickness on the wake were negligible considering a small ($\sim$10 %) variation in δ. In the current study, the change in δ/h remains within $\sim$10 %, which does not alter the submergence condition or lead to qualitative changes in flow behaviour. Further, a thick boundary layer ($\delta/h \geqslant 1$) was considered in the present study, which meant that the oncoming flow over the prism length played a significant role in dictating the wake characteristics through variations

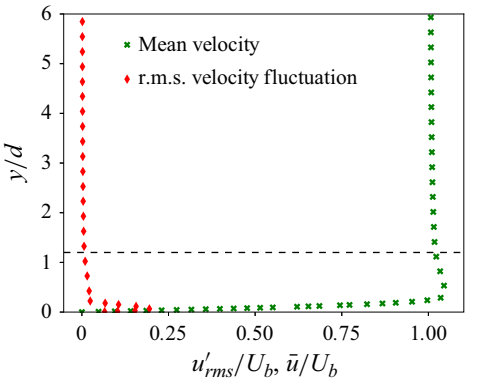

Figure 2. Distribution of the time-averaged and root-mean-square streamwise velocity ($\overline{u}$ and u'_{rms}) at the location of the leading edge of the prism at $Re = 2.5 \times 10^3$. Measurements were performed in the absence of the prism. Dashed line shows the boundary layer thickness (δ/d).

in the strength of the separated vortex sheet over the prism length (Bourgeois, Sattari & Martinuzzi 2011).

The second-order implicit backward Euler numerical scheme was employed for temporal discretisation, while the centeral difference scheme was used to approximate the diffusive and convective fluxes. Discretised equations were solved using the Pressure Implicit with Splitting Operator (PISO) algorithm (Goswami & Hemmati 2022). Time-marching simulations were performed with an adjusted temporal grid to maintain a maximum Courant number below 0.8, yielding a maximum time-step size of $\Delta t^* = \Delta t U_b/d = 0.001$. Further, the ratio of eddy-turnover time (τ_η) to Δt for the smallest dissipative eddies was ∼50. Each simulation completed 150 vortex shedding cycles, with data from the last 100 cycles used for post-processing. Simulations were completed on a Digital Research Alliance of Canada computing cluster, using 256 Intel $E5$-2683 v4 Broadwell cores with 125 GB of shared memory, requiring 6×10^5 core hours in total.

2.1. *Verification and validation*

Numerical simulations were verified by evaluating the sensitivity of the results to domain size and grid resolution. The set-up, domain and grid configuration were mimicked from our previous studies (Goswami & Hemmati 2022, 2023). For the domain size, we acknowledge that the present computational domain was designed to be larger than those employed in previous studies (Saha 2013; Rastan *et al.* 2021). Moreover, blockage ratio (β) and domain height (H) were set as 0.01 and $6d$, respectively, following the criteria of $\beta = (d \times h)/(W \times H) \leqslant 0.05$ and $H \geqslant h + 5d$, to ensure negligible effects of domain on the global flow features (Sohankar, Norberg & Davidson 1998; Saha 2013). This further ensures that both volumetric and directional confinement effects remain negligible across all simulations. Grid sensitivity was assessed using four successively refined grids with 5.1×10^6, 15.1×10^6, 19.6×10^6 and 25.2×10^6 elements. Sensitivity of the domain and grid on the global flow features, which are the mean drag coefficient ($\overline{C_d}$) and lift coefficient ($\overline{C_l}$), are presented in table 1, which indicate that Domain 2 ($30d \times 6d \times 12d$) was sufficient. Relative errors in the mean drag coefficient ($\overline{C_d}$) and lift coefficient ($\overline{C_l}$) between Grid 3 and Grid 4 were below 1 %, indicating grid convergence for Grid 3 as presented in table 1. As such, Domain 2 and Grid 3 were selected for the present study.

Study	N_{total}	Domain size	y^+_{max}	$\overline{C_d}$	$\lvert\Delta\overline{C_d}\,\%\rvert$	$\overline{C_l}$	$\lvert\Delta\overline{C_l}\,\%\rvert$
Domain 1	17.3×10^6	$30d \times 5d \times 10d$	0.8	1.102	5.60	0.921	5.14
Domain 2	19.6×10^6	$30d \times 6d \times 12d$	0.8	1.041	—	0.875	—
Domain 3	20.9×10^6	$35d \times 6d \times 12d$	0.8	1.043	0.19	0.876	0.10
Domain 4	38.6×10^6	$30d \times 12d \times 14d$	0.8	1.042	0.09	0.875	0.03
Grid 1	5.1×10^6	$30d \times 6d \times 12d$	3.1	1.100	5.51	0.914	5.33
Grid 2	15.1×10^6	$30d \times 6d \times 12d$	1.55	1.061	2.36	0.899	3.55
Grid 3	19.6×10^6	$30d \times 6d \times 12d$	0.8	1.041	0.38	0.875	0.90
Grid 4	25.2×10^6	$30d \times 6d \times 12d$	0.44	1.037	—	0.868	—

Table 1. Domain and grid sensitivity analysis results for wall-mounted prism with $DR = 4$ at $Re = 2.5 \times 10^3$. The relative error is calculated with respect to Domain 2 and Grid 4, respectively.

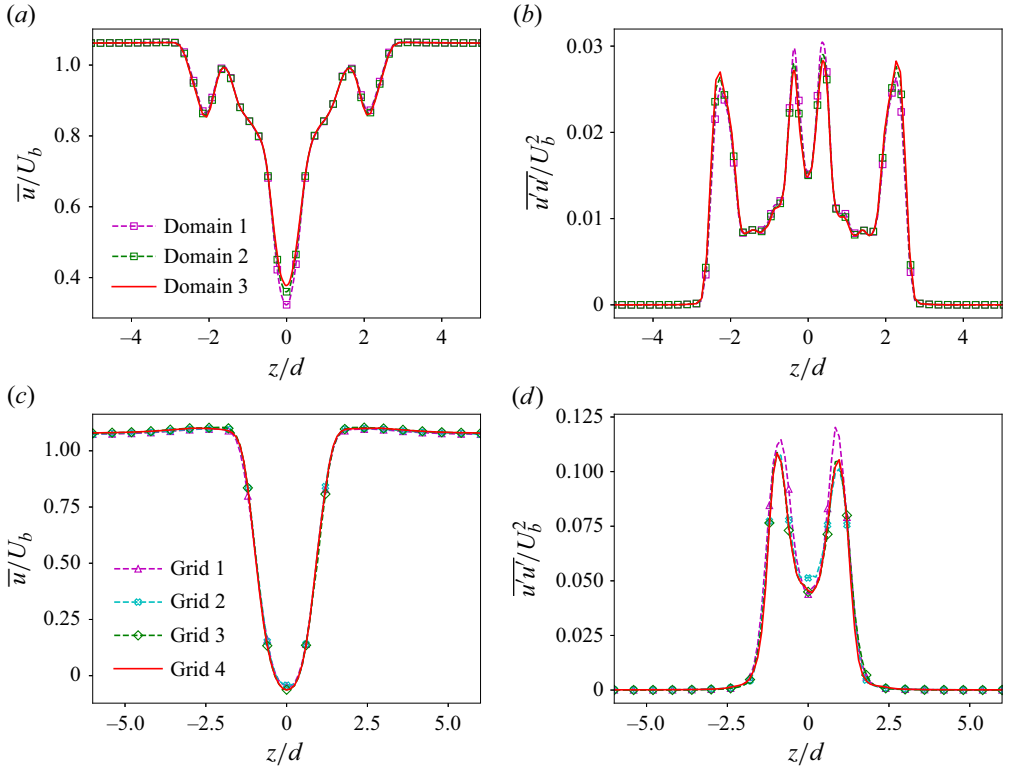

Figure 3. Effect of (*a*,*b*) domain and (*c*,*d*) grid sizes on mean and turbulent wake characteristics. Shown are (*a*,*c*) $\overline{u}$ and (*b*,*d*) $\overline{u'u'}$.

Further, the sensitivities of the domain and grid sizes were investigated on the mean and turbulent flow characteristics behind a wall-mounted prism with $DR = 4$ at $Re = 2.5 \times 10^3$. The results are presented in figure 3. Comparing the profiles of $\overline{u}$ and $\overline{u'u'}$, at $x/d = 1$ downstream of the prism for all domain sizes, there exists a close agreement between Domain 2 and Domain 3. The influence of blockage is further apparent in Domain 1, where the centreline velocity is significantly higher compared with other domains. Based on these results, it was confirmed that Domain 2 was sufficient to capture all relevent wake characteristics for this study. Similarly, grid sensitivity analysis revealed

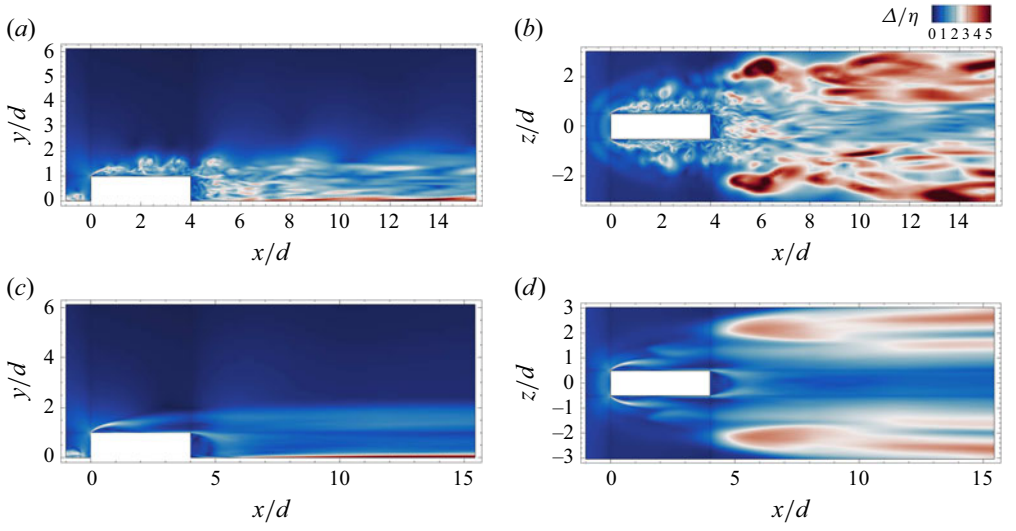

Figure 4. Contours of (*a*,*b*) instantaneous and (*c*,*d*) time-averaged (mean) distributions of the ratio of grid size to Kolmogorov length scale (Δ/η) in the (*a*,*c*) symmetry plane ($z/d = 0$) and (*b*,*d*) x–z plane ($y/d = 0.5$) for the case of $DR = 4$ at $Re = 2.5 \times 10^3$.

that Grid 3 was sufficient to capture the wake characteristics, with negligible influence of further grid refinement. Results in figures 3(*c*) and 3(*d*) show an excellent agreement between Grid 3 and Grid 4, with a maximum of 1 % deviation.

The present study necessitates the accurate resolution of the smallest resolvable flow features, such as the leading-edge shear layer and wake structures in the immediate vicinity of the prism. To this end, the grid size should be comparable to the Kolmogorov length scale (Moin & Mahesh 1998). Therefore, we investigated the ratio of grid size (Δ) to Kolmogorov length scale (η) for further verification. The Kolmogorov length scale was estimated using $\eta = (\nu^3/\varepsilon)^{1/4}$, where ε is the viscous dissipation rate defined by $\varepsilon = 2\nu\overline{S_{ij}S_{ij}}$, and S_{ij} was the strain-rate tensor (Pope 2001). The grid size is calculated as $\Delta = \sqrt[3]{\Delta x \times \Delta y \times \Delta z}$. Using direct numerical simulation, Yakhot *et al.* (2006) and Saeedi, LePoudre & Wang (2014) suggested $\Delta/\eta = 2{-}5$ in the critical regions of the wake of wall-mounted prisms. Additionally, Celik, Klein & Janicka (2009) and Rastan *et al.* (2021) recommended $20 \leqslant \Delta/\eta \leqslant 40$ for LES. Further, Cimarelli *et al.* (2018) suggested $\Delta/\eta < 2.2$ at the locaton of the leading-edge shear layer using direct numerical simulation (DNS), where the transitional mechanisms take place, and $\Delta/\eta < 6.2$ in the turbulence core region above the prism. Moreover, Cao *et al.* (2022) suggested that majority of turbulence kinetic energy is dissipated on a scale of $\Delta/\eta \approx 10$, which was a constraint used by most previous DNS studies.

As shown by the contours of Δ/η in figure 4, both instantaneous and time-average (mean) contours of Δ/η fell into the required range of $5{-}10$ discussed earlier. Particularly, the values of Δ/η for the mean field were smaller than 5, while region with $\Delta/\eta > 5$ in the instantaneous field only covered ∼8 % of the wake. Maximum Δ/η of ∼8.6 occured at $x/d = 15$, with $\Delta/\eta = 1{-}3$ in the immediate vicinity of the prism. A probability density histogram of Δ/η for the entire computational domain is presented in figure 6(*a*). These results further confirm that the majority of the flow is resolved with $\Delta/\eta < 5$. Further, a maximum Δ/η of 8.6 is well within the range of $5{-}10$ suggested by previous studies (Yakhot *et al.* 2006; Celik *et al.* 2009; Saeedi *et al.* 2014; Rastan *et al.* 2021). The mean value of $\Delta/\eta \approx 0.96$ fits well within the ratio suggested by Cimarelli *et al.* (2018),

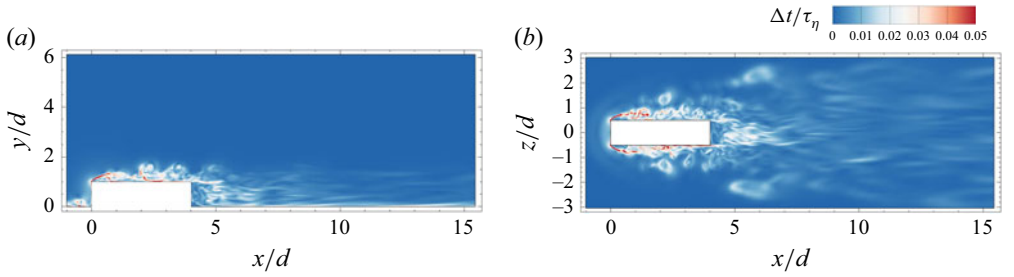

Figure 5. Contours of ratio between time step (Δt) and the Kolmogorov time scale (τ_η) for the instantaneous flow field in the (a) symmetry plane ($z/d = 0$) and (b) x–z plane ($y/d = 0.5$) for the case of $DR = 4$ at $Re = 2.5 \times 10^3$.

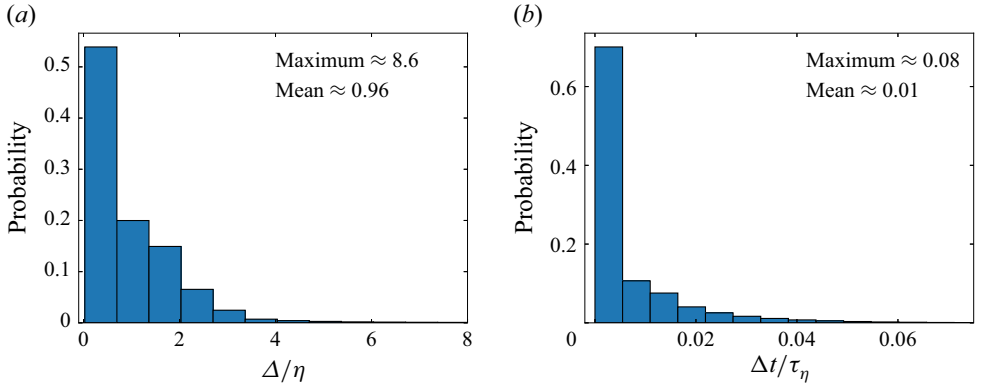

Figure 6. Histogram of the (a) ratio of grid size to Kolmogorov length scale (Δ/η) and (b) ratio of time-step size to the Kolmogorov time scale (τ_η) for the case of $DR = 4$ at $Re = 2.5 \times 10^3$. Histogram is presented for the instantaneous flow field in the entire computational domain.

indicating that the grid resolution is sufficient to capture the transitional mechanisms and shear-layer instabilities of the leading-edge shear layer. Together, results of Δ/η show that the resolution of Grid 3 is sufficient to capture the critical flow features behind the wall-mounted prisms.

The closeness between the smallest resolved time scales and Kolmogorov time scale (τ_η) determines the accuracy in resolving the fluctuations in turbulent flow, according to Moin & Mahesh (1998) and Li *et al.* (2020). As such, we investigated the ratio between the selected time step (Δt) and Kolmogorov time scale, given as $\tau_\eta = (\nu/\epsilon)^{1/2}$, to confirm the validity of the numerical set-up. Previously, Li *et al.* (2020) suggested that the mean time ratio ($\Delta t/\tau_\eta$) should be less than 0.0205 for a finely resolved time scale corresponding to ∼50 eddy-turnover times. Contours of $\Delta t/\tau_\eta$ are presented in figure 5 and the probability density of $\Delta t/\tau_\eta$ in the entire computational domain is presented in figure 6(b). The results in figure 6(b) show that the maximum and mean $\Delta t/\tau_\eta$ are 0.08 and 0.01, respectively, indicating that the time-step size is well within the range suggested by Li *et al.* (2020). Further, the majority (∼95 %) of the computational domain has $\Delta t/\tau_\eta < 0.02$, while only ∼0.5 % of the area confined to the leading-edge of the prism shows $0.02 \leqslant \Delta t/\tau_\eta \leqslant 0.06$. As shown in figure 5, $\Delta t/\tau_\eta \approx 0.05$ in the immediate vicinity of the prism, with average $\Delta t/\tau_\eta \approx 0.01$ in the wake region. The $\Delta t/\tau_\eta$ distribution, following the criterion of Li *et al.* (2020) and Duong *et al.* (2024), confirmed that temporal grid resolution was sufficient to capture the small-scale turbulent fluctuation in the present study.

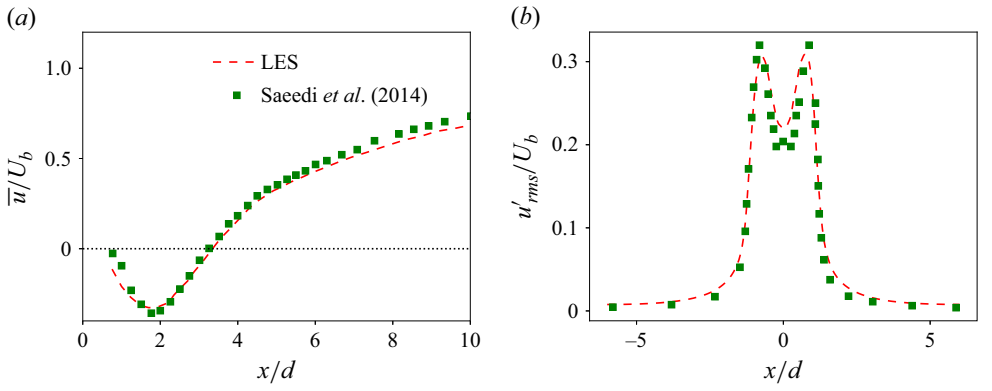

Figure 7. Comparison of (*a*) mean axial velocity ($\overline{u}$) and (*b*) root-mean-squared velocity (u'_{rms}) profiles obtained from LES with the experimental results of Saeedi *et al.* (2014).

The lack of existing experimental data for our specific case (prism with $DR = 4$, $Re = 2.5 \times 10^3$) forced us to adopt an alternate validation approach. We mimicked the set-up of Saeedi *et al.* (2014) for a prism with $AR = 4$ and $Re = 1.2 \times 10^5$ using LES. Grid resolution and computational set-up mirrored that of the present study. Mean axial velocity profiles from LES agreed well with Saeedi *et al.* (2014), such that we had less than 5 % deviation (figure 7*a*). Figure 7(*b*) further shows satisfactory agreement between LES and experiments in capturing the root-mean-squared velocity profiles. The trends at the peak and into the wake are well reproduced by the numerical simulations. This outcome validated our numerical set-up.

3. Results and discussion

First, the main features of the instantaneous wake are analysed qualitatively. Figure 8 displays the instantaneous three-dimensional vortex structures for prisms with $DR = 1$ and 4 and $AR = 1$ and 1.5 at $Re = 2.5 \times 10^3$. The sharp leading edge of the prism fixes the boundary layer detachment point, leading to the formation of a leading-edge shear layer. This shear layer undergoes distinct stages of growth and onset of primary instabilities (Moore *et al.* 2019*a*). A Kelvin–Helmholtz instability first develops, resulting in the formation of finite spanwise vortex rollers near the leading edge, as shown in figure 8. A secondary instability associated with KHI then destabilises these spanwise rollers, resulting in the formation of hairpin-like vortices downstream. For both aspect ratios, the long prism ($DR = 4$) exhibits prominent spanwise vortex shedding and formation of hairpin-like vortices over the prism surfaces. In contrast, the leading-edge shear layer sheds directly into the wake for the short prism ($DR = 1$), triggering secondary instabilities described by Goswami & Hemmati (2022), which suppress vortex shedding. This suppression is evident in figure 8, where the long prism ($DR = 4$) shows more prominent spanwise vortex shedding compared with the short prism ($DR = 1$). In this study, the term 'long prism' refers to $DR = 4$ and 'short prism' refers to $DR = 1$.

Figure 9 illustrates instantaneous vortex structures for prisms with $DR = 1$ and 4 at $Re = 5 \times 10^3$ and 1×10^4. Results indicate that vortex shedding becomes more pronounced at higher Reynolds numbers, with the long prism displaying notably stronger spanwise vortex shedding compared with the short prism. Additionally, vortex shedding is more irregular at higher Reynolds numbers than $Re = 2.5 \times 10^3$ (see figure 8). These observations in figure 9 confirm the impact of prism depth ratio on flow irregularity and vortex shedding

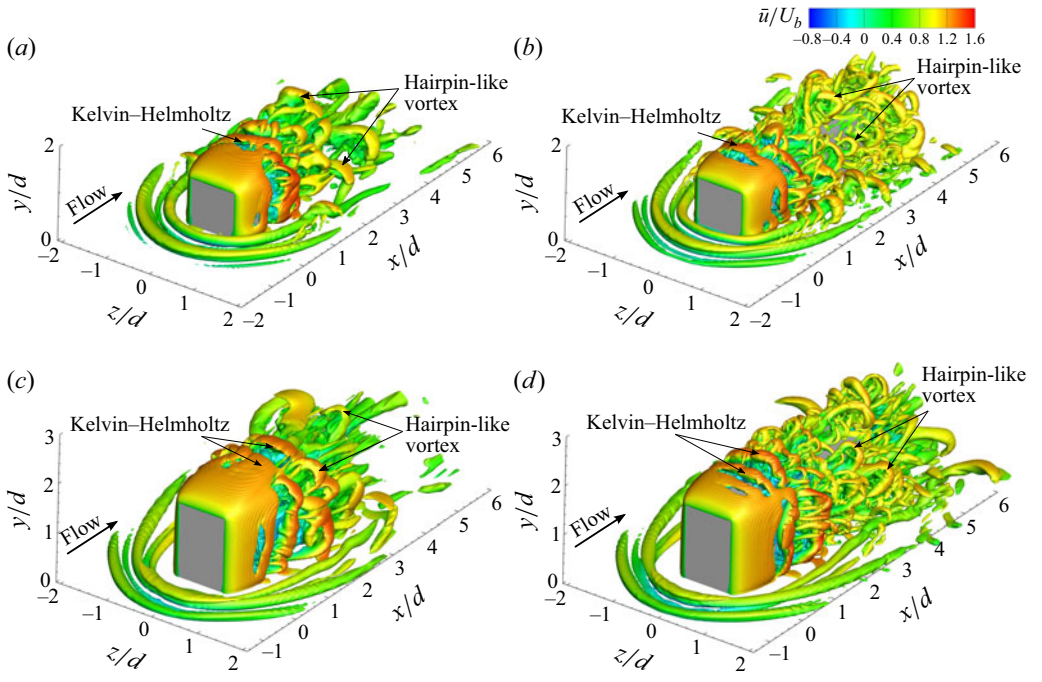

Figure 8. Instantaneous vortex structures overlaid with axial velocity (u) contours for (a,c) $DR = 1$ and (b,d) $DR = 4$ prisms with (a,b) $AR = 1$ and (c,d) $AR = 1.5$ at Reynolds number of 2.5×10^3, identified using Q-criterion ($Q^* = 1$).

characteristics at elevated Reynolds numbers. Onset of Kelvin–Helmholtz instability is observed near the leading edges of both prisms, resulting in the formation of spanwise KHI rollers. At higher Reynolds numbers, these KHI rollers form closer to the leading edge. However, downstream formation of hairpin-like vortices and the overall spanwise vortex shedding pattern remain consistent with those at $Re = 2.5 \times 10^3$.

While previous studies have scrutinised the vortex shedding mechanism for infinite-span rectangular prisms (Cimarelli *et al.* 2018; Zhang *et al.* 2023), there are no studies that focus on quantitative investigation of the onset of KHIs and subsequent enhancement of the wake irregularity for finite-span prisms. Moreover, previous studies have discussed the evolution of leading-edge vortex rollers for infinite-span rectangular prisms. However, there has been limited attention given to destabilisation of the leading-edge shear layer. Since the wake of finite wall-mounted prisms is impacted by various end-effects (Wang & Zhou 2009), the source of unsteadiness in the leading-edge shear layer remains unclear. Moreover, Zargar *et al.* (2022) examined the transitional mechanism and early wake developments behind long prisms ($DR \geqslant 3$), suggesting that hairpin-like vortices form after the initial shear-layer roll-up. Preliminary results, however, show that a destabilisation mechanism deforms the spanwise roller following the initial shear-layer roll-up, which subsequently form hairpin-like structures. Thus, this work aims to address this knowledge gap by investigating the mechanism of destabilisation in the leading-edge shear layer at increasing depth ratio.

3.1. *Mean flow characteristics*

The main features of the mean flow topology are discussed in this section to provide a comprehensive understanding of the flow characteristics around wall-mounted prisms. Figures 10(a) and 10(b) present mean streamwise velocity ($\overline{u}$) contours overlaid with

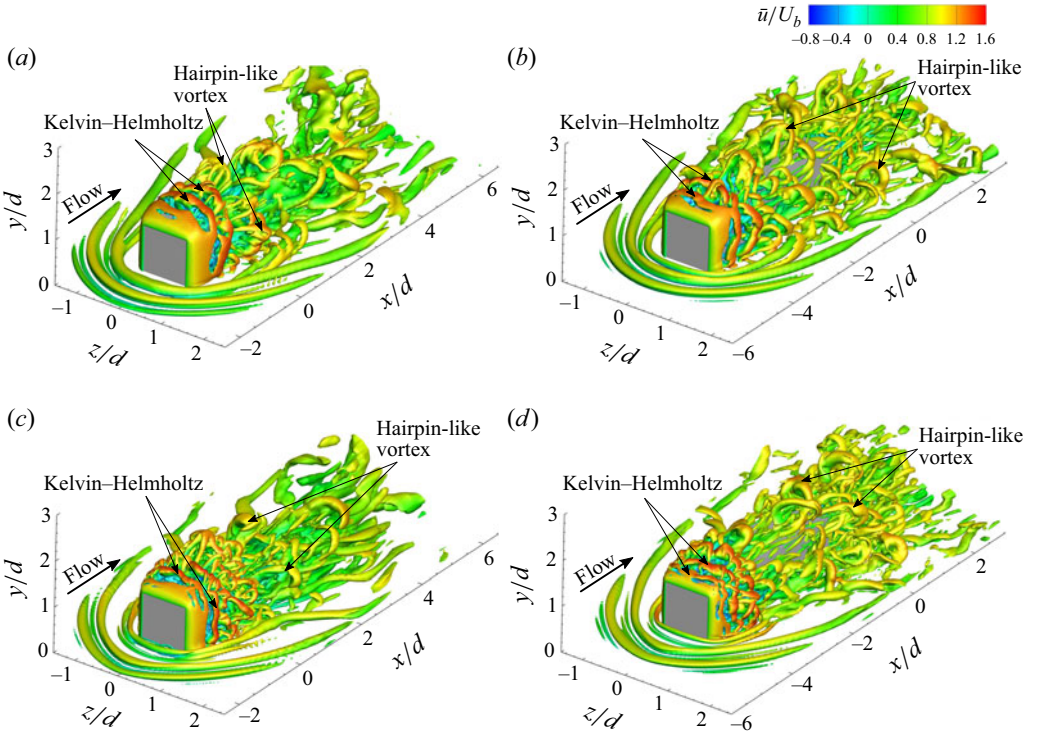

Figure 9. Instantaneous vortex structures overlaid with axial velocity (u) contours for (a,c) $DR = 1$ and (b,d) $DR = 4$ prisms at (a,b) $Re = 5 \times 10^3$ and (c,d) $Re = 1 \times 10^4$, identified using Q-criterion ($Q^* = 1$).

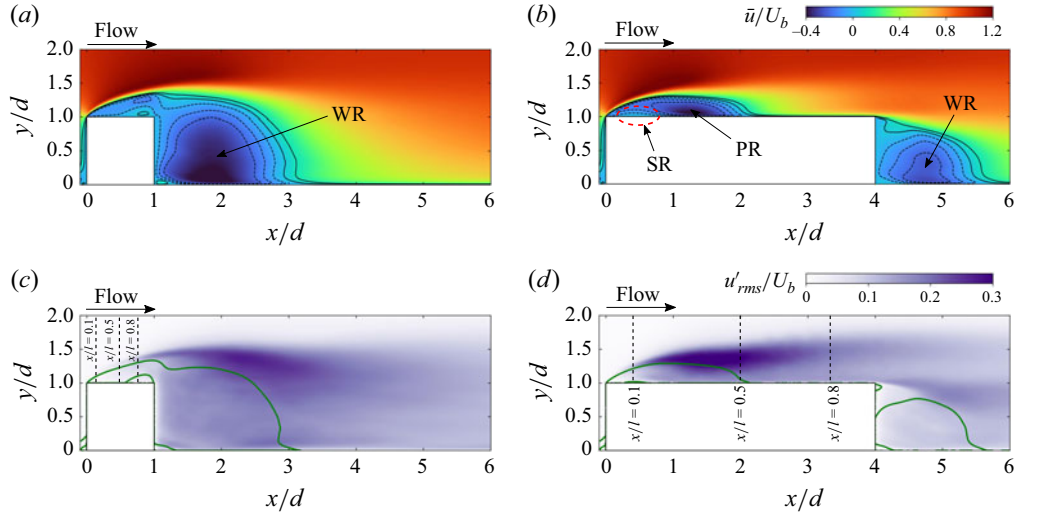

Figure 10. (a,b) Mean streamwise velocity ($\overline{u}$) contours overlaid with mean velocity streamlines; and (c,d) contours of root-mean-squared streamwise fluctuations (u'_{rms}) overlaid with streamline of $\overline{u} = 0$. Contours presented for (a,c) $DR = 1$ and (b,d) $DR = 4$ prisms at $Re = 2.5 \times 10^3$ at spanwise plane of $z/d = 0$.

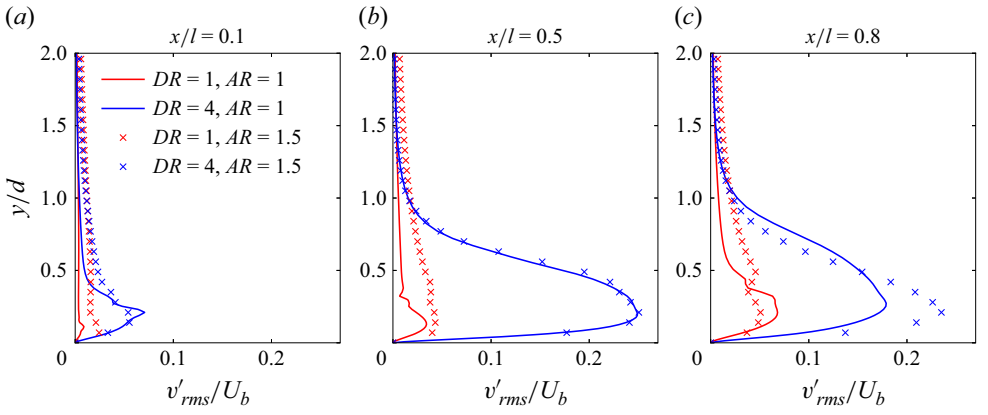

Figure 11. Profiles of root-mean-squared normal velocity fluctuations (v'_{rms}) at different streamwise locations shown in figures 10(*c*) and 10(*d*) for (red) $DR = 1$ and (blue) $DR = 4$ prisms at $Re = 2.5 \times 10^3$. Solid lines show profiles for $AR = 1$ prisms, while the $\times$ markers indicate the profiles for $AR = 1.5$ prisms.

mean velocity streamlines for both prisms, highlighting flow separation at the leading edge. For the short prism, the leading-edge shear layer extends into the wake, forming a wake recirculation (WR) region. For $DR = 4$, the shear layer reattaches to the top surface of the prism at $x/d \approx 2.12$, creating a primary recirculation (PR) region on the top surface. Additionally, a secondary recirculation (SR) region forms below the PR region, due to the reverse flow induced by the near-wall region of the PR, resulting in an upstream-moving boundary layer. For the short prism, PR and SR regions are absent due to a lack of flow reattachment on the prism surfaces. On the upper surface of the prism, particularly for high-depth-ratio cases, a localised recirculation loop develops in the range $x/l = 0.6$ to 1. This flow region exhibits upstream-directed velocity due to the presence of a secondary recirculation zone. The resulting streamline pattern forms a counterclockwise loop (in side-view), caused by reverse flow and reattachment of the separated shear layer. This represents part of the feedback mechanism that drives the destabilisation of the leading-edge shear layer. Figures 10(*c*) and 10(*d*) show contours of root-mean-squared streamwise fluctuations (u'_{rms}) overlaid with the $\overline{u} = 0$ streamline (in green) for both prisms. These figures indicate that the initial leading-edge shear layer exhibits laminar characteristics. However, velocity fluctuations intensify with the onset of KHI vortex rollers and their subsequent interactions (Goswami & Hemmati 2024), marking the transition to turbulence. Regions of intense fluctuations show high turbulence intensity (u'_i) and maximum turbulence kinetic energy ($u'_i u'_i$). For $DR = 1$, u'_{rms} intensifies near the WR region and then gradually declines downstream. For $DR = 4$, u'_{rms} amplification is more pronounced near the PR region with another peak near the WR region, coinciding with trailing-edge flow separation.

Figure 11 shows profiles of the root-mean-squared normal velocity fluctuations (v'_{rms}) at different streamwise locations immediately downstream of the leading edge for both prisms (shown in figures 10*c* and 10*d*), comparing the profiles for aspect ratios $AR = 1$ and 1.5. Streamwise locations are normalised by the prism length (l) to facilitate comparison between prisms of different depth ratios. This comparison reveals that wake oscillation intensity is significantly higher for $DR = 4$ than $DR = 1$. Additionally, wake oscillation intensity reaches a peak at $x/l = 0.5$ for $DR = 4$, corresponding to the location of leading-edge shear-layer reattachment. This confirms that the wake strength is influenced by the prism depth ratio, as flow separation and reattachment vary across surfaces. The long

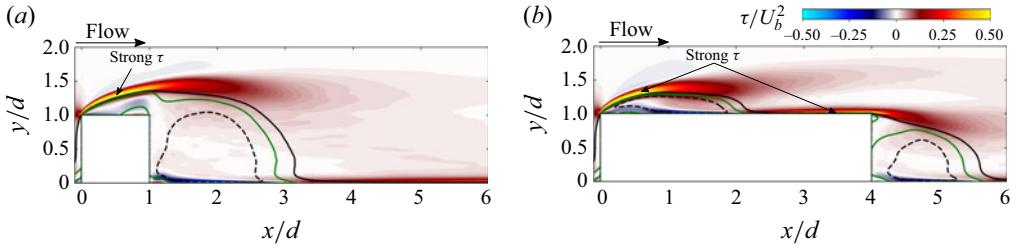

Figure 12. Mean shear (τ) at leading edge of (*a*) $DR = 1$ and (*b*) $DR = 4$ prisms with $AR = 1$ at $Re = 2.5 \times 10^3$. Contours are overlaid with streamline of $\overline{u} = 0$ (green) and critical streamlines (black).

prism shows stronger velocity fluctuations (v'_{rms}) compared with the short prism, further highlighting the role of depth ratio in enhancing wake irregularity. Similar conclusions are apparent from comparisons of prisms with $AR = 1.5$, where the longer prism ($DR = 4$) displayed a stronger wake compared with $DR = 1$.

Figure 12 presents contours of the mean shear stress, defined as $\tau = \mu(\partial\overline{u}/\partial y)$. Results highlight strong τ at the leading edge of both prisms, while intensity of τ rises with increasing depth ratio, leading to a greater overall shear stress. Additionally, a region of intense mean shear flow is observed near the trailing edge for the longer prism ($DR = 4$), where the leading-edge shear layer reattaches and separates again. The stronger mean shear stress associated with the higher depth-ratio prism significantly influences the inception and development of hairpin-like vortices. For example, Zhang *et al.* (2023) demonstrated that hairpin vortex formation is driven by the background mean shear flow with regions of high shear stress forming the vortex head in high-momentum zones, while low-momentum regions form vortex legs.

3.2. *Onset of Kelvin–Helmholtz instability*

The onset of Kelvin–Helmholtz instability vortex roll-up depends on the prism depth ratio (Goswami & Hemmati 2024). For $DR = 1$, vortex tubes extend into the downstream wake region, whereas they appear over the prism surfaces for $DR = 4$. Similar vortex tubes are observed along side surfaces of both prisms. Following this, streamwise vortex tubes undergo modulation in the spanwise direction, the locations of which align with the local maxima of mean shear stress (figure 12). Under the influence of strong mean shear flow, modulated vortex tubes are stretched and roll-up into hairpin-like vortices, arranged in a staggered formation, which are shed downstream. Figure 13 illustrates the pattern adopted by the streamwise vorticity (ω_x), highlighting the flow motion and development of streamwise vortices, which induce flow entrainment due to high- and low-speed streaks (Jimenez 1983). At high Reynolds numbers, similar high- and low-speed streaks appear (see figures 13*c* and 13*d*). Flow entrainment is particularly evident near the leading edge of the long prism with streamwise vortices extending into the wake region. In contrast, streamwise vortices emerge well into the wake for $DR = 1$. These observations suggest that flow entrainment is more pronounced near the leading edge for the long prism compared with the short prism.

Instantaneous vortex shedding is closely examined near the leading edge of both prisms, in figure 14, which includes contours of spanwise vorticity (ω_z^*) overlaid with instantaneous streamlines and $\overline{u} = 0$ isopleth at $z/d = 0$. In both cases, the generation of Kelvin–Helmholtz-like vortices from the leading edge is notable. A zoomed-in sub-figure near the leading edge in figure 14 reveals an earlier initiation of Kelvin–Helmholtz instability for $DR = 4$ compared with $DR = 1$, where the instability appears further

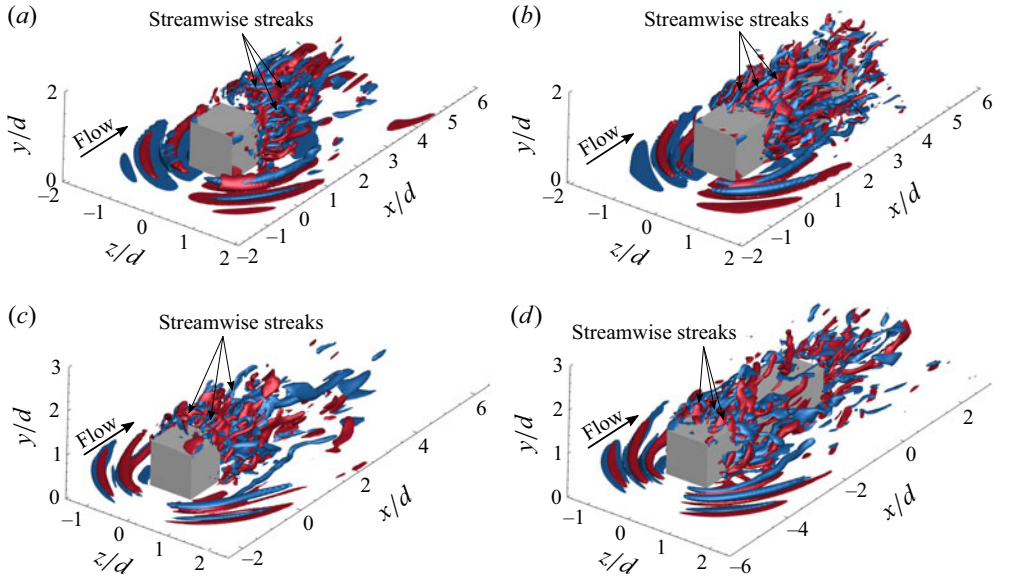

Figure 13. Iso-surfaces of streamwise vorticity, $\omega_x^* = \pm 5$, at (*a*,*b*) $Re = 2.5 \times 10^3$ and (*c*,*d*) $Re = 1 \times 10^4$ for (*a*,*c*) $DR = 1$ and (*b*,*d*) $DR = 4$ prisms.

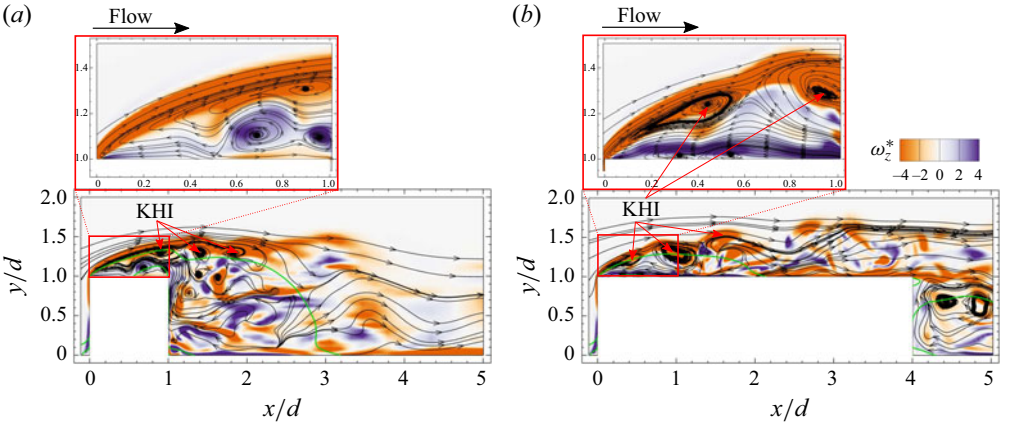

Figure 14. Contours of span-wise vorticity, ω_z^*, for (*a*) $DR = 1$ and (*b*) $DR = 4$ at Reynolds number of 2.5×10^3, superimposed with instantaneous streamlines and the isopleth of $\overline{u} = 0$ (bold, green line) at $z/d = 0$.

downstream at $x/d \geqslant 1$. For the former, streamlines show flow entrainment near the prism top surface, characterised by a region of positive ω_z^* and an upstream trajectory. This entrainment is less pronounced for $DR = 1$. For $DR = 4$, flow entrainment from the primary recirculation bubble impinges on the top surface, leading to the formation of two boundary layers: one moving upstream and the other downstream (Cimarelli *et al.* 2018). Downstream flow structures predominantly align in the streamwise direction, as shown in figure 13(*b*). Conversely, upstream-moving structures form a strong region of positive ω_z^* (see figure 14), corresponding to spanwise-aligned flow structures reminiscent of vortex tubes aligned in the spanwise direction. This region of positive ω_z^* may be the source of

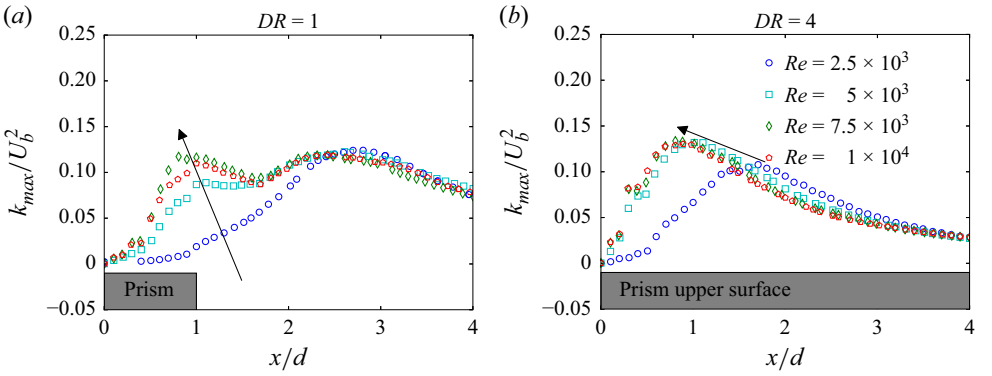

Figure 15. Downstream trajectory of maximum turbulence kinetic energy (k_{max}) along the prism mid-span ($z/d =$) for (*a*) $DR = 1$ and (*b*) $DR = 4$ prisms. Leading edge of the prisms (shown in grey) is located at $x/d = 0$.

undulations forming on the vortex tubes near the leading edge. Further investigation is presented later in this study.

The onset of Kelvin–Helmholtz instability and subsequent formation of hairpin-like vortices are further analysed by tracking the downstream trajectory of maximum turbulent kinetic energy (k_{max}) along the prisms mid-span ($z/d = 0$). Based on the dynamics described in prior studies (Moore *et al.* 2019*a*,*b*), turbulent kinetic energy is expected to increase in amplitude as fluctuations grow downstream of the leading edge. This implies that the trajectory of k_{max} could align with the path of the leading-edge shear layer and the subsequent vortex shedding. Figure 15 shows the downstream trajectory of k_{max} for both prisms. At $Re = 2.5 \times 10^3$, k_{max} grows rapidly for both prisms, starting near zero at the leading edge, where flow separation occurs. For $DR = 1$ at $Re = 2.5 \times 10^3$, k_{max} reaches a maximum in the wake at $x/d \approx 2.8$, after which it saturates and drops. Increasing Reynolds number shifts this saturation point upstream, closer to the prism trailing edge. At higher Reynolds numbers, a secondary peak in k_{max} appears in the wake, primarily due to the wake interactions (see figure 10*c*), resulting in increased momentum transport. Similar upstream shifts in the onset of Kelvin–Helmholtz instability at higher Reynolds number have been observed in previous studies, notably by Moore *et al.* (2019*a*) and Cimarelli, Corsini & Stalio (2024).

For the long prism, a similar trend is observed, where k_{max} rapidly increases from near zero at the leading edge towards a maxima close to the shear-layer reattachment location on the top surface. The shift in the peak of k_{max} is more pronounced for the long prism than the short prism, indicating a more intense growth of turbulence intensities. Following the flow reattachment, k_{max} decreases moving downstream. Near the leading edge, k_{max} is significantly higher for the long prism compared with the short prism, indicating greater turbulence intensity, consistent with the results in figures 10(*c*) and 10(*d*). The saturation point of k_{max} has been linked in previous studies (Moore *et al.* 2019*a*) to the onset of Kelvin–Helmholtz instability. This implies that the onset of Kelvin–Helmholtz instability shifts upstream with increasing Reynolds numbers for wall-mounted prisms. At higher Reynolds numbers, a self-similarity trend is observed in k_{max} for both prisms, which is more pronounced for the long prism with trends of k_{max} converging at $Re = 5 \times 10^3$. Although this trend is not observed for the short prism within the current range of Reynolds numbers, it is reasonable to hypothesise that extending Re beyond 1×10^4 could yield a similar effect, based on analogous behaviours observed in comparable geometries at higher Reynolds numbers (Moore *et al.* 2019*a*,*b*). Self-similarity of k_{max}

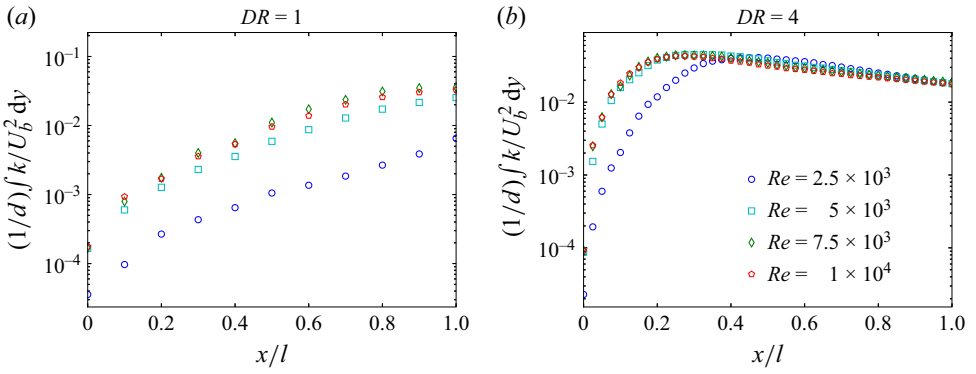

Figure 16. Integrated turbulence kinetic energy along the prism mid-span ($z/d =$) for (a) $DR = 1$ and (b) $DR = 4$ prisms. Axial length is normalised by the prism length (l).

at higher Reynolds numbers suggests a Reynolds number invariant behaviour, indicating that turbulence intensities are primarily influenced by depth ratio (prism geometry) at high Re.

Vorticity in the flow is generated under the influence of non-uniform pressure gradient along the prism length, while turbulent kinetic energy is generated by fluctuations in the presence of a mean velocity gradient (Pope 2001). Integrated turbulent kinetic energy downstream of the leading edge reflects the cumulative amount at any given location, which can be used to quantitatively track the growth of turbulence intensity (Moore *et al.* 2019*a*). Figure 16 presents the integrated turbulent kinetic energy along the prism mid-span ($z/d = 0$) for both prisms, which shows its rise downstream of the leading edge for both cases. This indicates a substantial turbulence production. Growth rate of turbulent kinetic energy is more pronounced along the long prism compared with the short prism, suggesting pronounced flow irregularity. Increased unsteadiness near the leading edges is attributed to flow reattachment on surfaces of the long prism, leading to a rise in turbulence intensity (figure 15*b*). These results quantitatively indicate that turbulence intensity is significantly higher for the long prism than short prism, highlighting that depth ratio strongly influences the overall flow unsteadiness.

3.3. *Flow periodicity and dominant frequencies*

Inherent instabilities in the flow give rise to distinct frequencies associated with specific physical flow phenomena. This section investigates flow periodicity and analyses the flow processes corresponding to these frequencies. Figure 17 presents the pre-multiplied power spectral density of streamwise (E_u) velocity fluctuations near the leading edge at (0.5, 1.3, 0) for both prisms. The results show that two dominant frequencies characterise the flow, corresponding to large-scale vortex shedding and Kelvin–Helmholtz instability. Large-scale vortex shedding frequency occurs at $St_{sh} \approx 0.17$ for both prisms, while frequencies of Kelvin–Helmholtz instability are $St_{kh} \approx 0.855$ and 1.290 for $DR = 1$ and 4, respectively. Similar observations are made at higher Reynolds numbers, where frequencies of large-scale vortex shedding remain constant for both prisms, while the frequency associated with KHI increases. For larger depth ratios, the frequency of KHI rises, indicating a stronger influence of KHI downstream of the leading edge (Goswami & Hemmati 2024). A tertiary frequency, noted at $St_{fb} \approx 0.59$ for the long prism at $Re = 2.5 \times 10^3$, is attributed to the feedback frequency from the secondary recirculation region to the primary recirculation region. Similar fractional harmonics (St_{fb}), corresponding

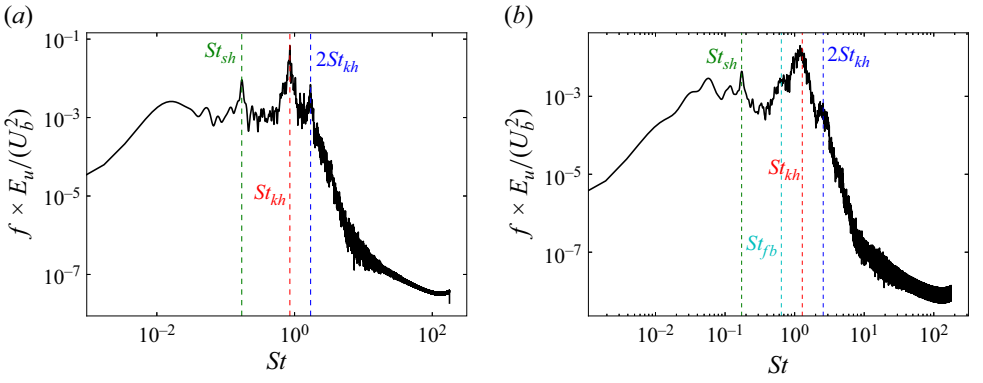

Figure 17. Pre-multiplied power spectral density of streamwise (E_u) velocity fluctuations near the leading edge at (0.5, 1.3, 0) for (*a*) $DR = 1$ and (*b*) $DR = 4$.

to the feedback of the impinging leading-edge shear layer, were observed previously for suspended prisms (Zhang *et al.* 2023). However, such feedback frequencies have not been reported in the literature for wall-mounted prisms. Therefore, flow mechanisms related to this frequency are further explored here.

Topological structures corresponding to large-scale vortex shedding and KHI frequencies are next analysed using Dynamic Mode Decomposition (DMD). This technique provides a computational framework to extract a primary low-order description of the data-set through its orthonormal modes in a temporal sense (Zheng *et al.* 2019; Khalid *et al.* 2020; Taira *et al.* 2020). In other words, DMD enables identification of spatial structures with characteristic frequencies associated with these structures. In the present study, DMD is applied to sequential flow-field snapshots of instantaneous velocity data to isolate dynamically dominant modes associated with shear-layer instabilities and wake oscillations. The decomposition yields mode shapes and growth rates, enabling a clear distinction between the leading-edge Kelvin–Helmholtz rollers and the large-scale trailing-edge vortices. Furthermore, spectral peaks from the DMD eigenvalue distribution are used to determine modal frequencies, which are cross-validated with fast Fourier transform-based power spectral density (PSD) analysis of velocity time signals. This approach allows for a more robust interpretation of the physical mechanisms driving unsteadiness and provides insights into the spatial origin and evolution of key instabilities. Additionally, the spatial coherence of DMD modes facilitates identification of modal interactions and energy pathways between the shear layer and recirculating wake regions, which are critical to understanding the observed destabilisation mechanisms.

Figure 18 presents contours of the real part of DMD modes for the streamwise component, corresponding to the shear layer and KHI for short and long prisms at $Re = 2.5 \times 10^3$. Figures 18(*a*) and 18(*c*) show structures associated with the large-scale vortex shedding frequency, displaying alternating streamwise structures arranged in a regular pattern. These structures originate near the location of shear-layer reattachment for $DR = 4$ and in the wake for $DR = 1$. Since large-scale vortex shedding mainly consists of hairpin-like vortices that shed from the breakdown of the leading-edge shear layer (Zhang *et al.* 2023), structures in figures 18(*a*) and 18(*c*) correspond to the onset of hairpin-like vortex shedding in the wake. These structures are more pronounced for the long rather than short prisms, indicating a more substantial growth of large-scale vortex shedding for the former.

Figures 18(*b*) and 18(*d*) show structures associated with the KHI frequency. These structures feature spanwise vortex tubes aligned in the streamwise direction, shedding from

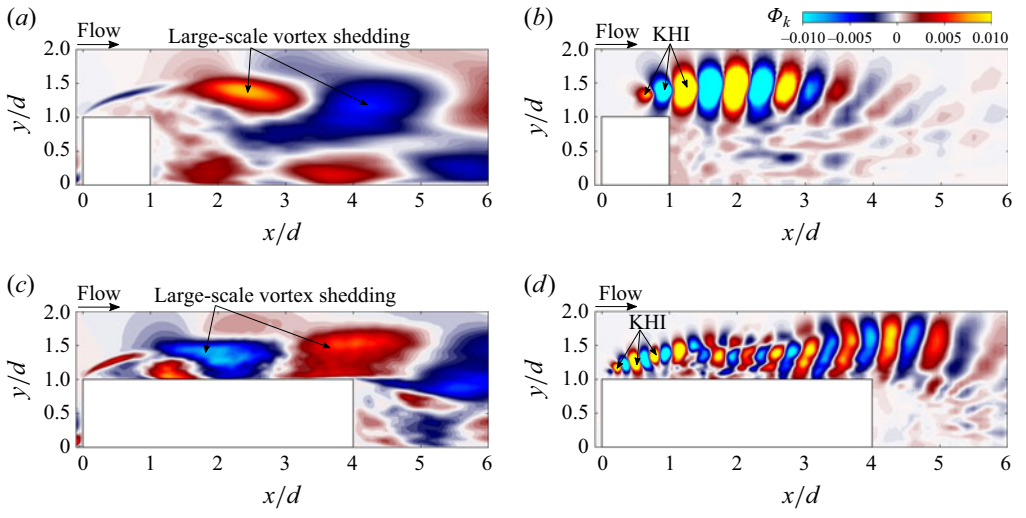

Figure 18. Contours of the real part of the DMD mode for streamwise component, corresponding to (*a*,*c*) shear layer and (*b*,*d*) Kelvin–Helmholtz instability for (*a*,*b*) $DR = 1$ and (*c*,*d*) $DR = 4$ prism at $Re = 2.5 \times 10^3$.

the leading-edge shear layer. In both cases, structures initiate near the leading edge, with the onset of KHI occurring closer to the leading edge for the long prism than for the short prism, consistent with figure 14. For the short prism, KHI structures decay rapidly into the wake and vanish downstream. In contrast, KHI structures persist further downstream and interact with the wake for the long prism. This interaction region is visible in figure 18(*d*) for the long prism, where KHI structures engage with the primary recirculation bubble and large-scale vortex shedding. Following this interaction, KHI structures destabilise and evolve into hairpin-like vortices that shed into the wake. Similar interactions were quantified by Goswami & Hemmati (2024), where KHI structures were shown to interact with large-scale vortex shedding.

3.4. *Mechanism of destabilisation of leading-edge shear layer*

Before discussing the mechanism of leading-edge shear-layer destabilisation, it is helpful to briefly review the main characteristics of separating and reattaching flow over wall-mounted prisms with varying depth ratios. For a cube ($DR = 1$), the flow is characterised by a shear layer that separates at the leading edge and extends into the wake, as shown in figure 10(*a*). In this case, downstream WR exhibits increased turbulence intensity and large-scale vortex shedding. For a long prism, the flow separates at the leading edge and reattaches on the prism top surface, forming a PR, as illustrated in figure 10(*b*), which features large unsteady fluctuations and spanwise vortex shedding. Shear layer reattachment also generates an SR region beneath the PR, characterised by reverse flow and an upstream-moving boundary layer. Destabilisation of the leading-edge shear layer occurs in the PR, leading to the formation of hairpin-like vortices that shed into the wake. Immediately downstream of the leading-edge separation, flow instabilities lead to the formation of spanwise structures, as shown in figure 8(*b*). Interactions between spanwise structures and the strong shear flow (figure 12 *b*) result in a spanwise modulation of vortex structures. This modulation stretches structures in the streamwise direction, forming hairpin-like and streamwise vortices, as observed in figure 13(*b*). Two branches of turbulent structures emerge: one moves downstream as detached fluctuations into the

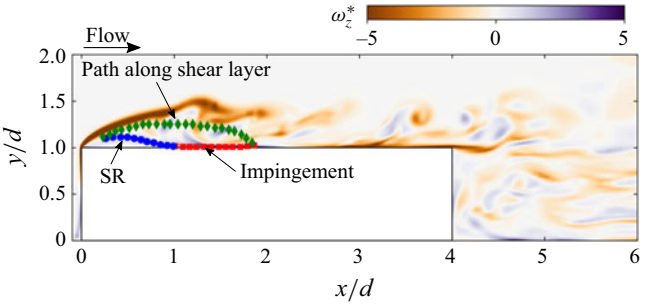

Figure 19. Contours of spanwise vorticity (ω_z^*) overlapped with critical streamline representing the recirculating region, at $Re = 2.5 \times 10^3$ for $DR = 4$ prism.

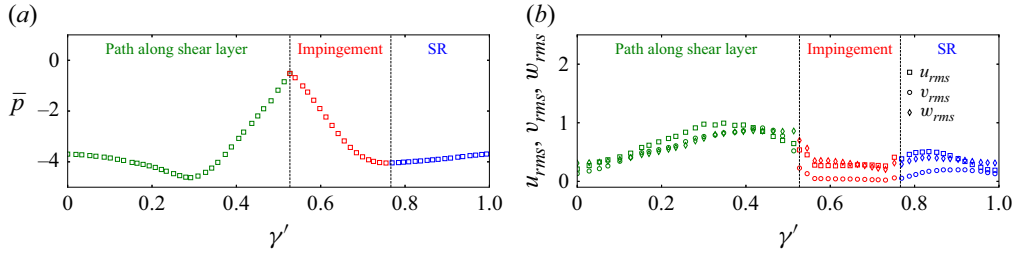

Figure 20. Trends of (*a*) pressure and (*b*) root-mean-squared velocity fluctuations (u'_{rms}, v'_{rms}, w'_{rms}) along the recirculating region for $DR = 4$ prism at $Re = 2.5 \times 10^3$. γ' represents the normalised curvilinear coordinate length.

wake, while the other impinges on the wall, moving upstream towards the leading edge and forming the secondary recirculation region.

The destabilisation mechanism in long prisms leads to increased flow irregularity and modulation of spanwise vortex structures. Results for the long prism are only considered to retain the focus in this study. The main analysis is performed along the two critical streamlines identified in figure 12(*b*). The first critical streamline represents the recirculating flow region formed by the shear-layer reattachment and it will be referred to as the 'recirculating region'. Following the methodology of Cimarelli *et al.* (2018), we analye flow statistics along the curvilinear coordinate length (γ), defined by the mean velocity streamline ($\gamma = \int \mathrm{d}\gamma$, where $\mathrm{d}\gamma = \sqrt{\mathrm{d}x^2 + \mathrm{d}y^2 + \mathrm{d}z^2}$), this path ($\gamma$) enables studying flow in PR and SR regions, and interactions between the leading-edge shear layer and the SR region. The second critical streamline, referred to as the 'path following free shear layer', enables analysis of the flow along the free shear layer and its development towards the free flow.

3.4.1. *Path following recirculation region*

The critical streamline that represents the recirculating region is shown in figure 19, overlaid with contours of spanwise vorticity (ω_z^*). For easier understanding of the flow dynamics, this recirculating region is divided into three sub-regions: (1) the area between shear-layer separation and reattachment (highlighted in green); (2) the impinging flow region and the branch of flow moving upstream (in red); and (3) secondary recirculation (SR) region below the primary recirculation (PR) region (in blue). Figure 20 shows trends of pressure and root-mean-squared velocity fluctuations (u'_{rms}, v'_{rms}, w'_{rms}) along the recirculating region depicted in figure 19. Following flow separation at the leading

edge, mean pressure decreases until it reaches the primary vortex core in the PR region at $\gamma' \approx 0.3$. Pressure then rises downstream, peaking at the shear-layer reattachment location ($\gamma' \approx 0.5$) on the prism top surface. This increase in pressure indicates a significant adverse pressure gradient, contributing to the formation of the PR. Beyond this point, pressure drops along the impingement region, moving upstream into the reverse boundary layer. Subsequently, mean pressure exhibits a favourable gradient, nearing the free stream pressure as the flow enters the SR. Here, pressure shows another adverse gradient as it moving back towards the leading edge.

Figure 20(*b*) shows trends of the root-mean-squared velocity fluctuations (u'_{rms}, v'_{rms}, w'_{rms}). Along the leading-edge shear layer (green symbols), velocity fluctuations increase due to the amplification of instabilities and transition to turbulence (Goswami & Hemmati 2024). Streamwise velocity fluctuations are most prominent here, reaching their maximum near the primary vortex core. Spanwise and normal fluctuations display similar intensities, with slightly larger spanwise fluctuations near the primary vortex core. Following this, normal and streamwise velocity fluctuations drop sharply until flow reattachment at $\gamma' \approx 0.5$, while spanwise fluctuations continue to increase. This results in maximised spanwise fluctuations near the shear-layer reattachment, suggesting the presence of intense spanwise vortex structures in this area. This is evident by the presence of spanwise KHI rollers in figure 8(*b*). In the impingement and reverse boundary layer regions (red symbols), overall velocity fluctuations drop sharply. Along the impingement region ($0.55 \leqslant \gamma' \leqslant 0.75$), normal velocity fluctuations become negligible, while streamwise and spanwise fluctuations remain steady. This indicates the formation of intense streamwise and spanwise structures, and the presence of spanwise sweeping of flow structures at impingement. Finally, normal velocity fluctuations increase in the SR (blue symbols), while streamwise and spanwise fluctuations rise sharply until reaching a local maximum near the secondary vortex core. Beyond this point, streamwise fluctuations decrease rapidly, while spanwise and normal fluctuations remain steady, closing the loop of the secondary recirculation region.

Pressure fluctuations (p') are influenced by velocity fluctuations (u', v' and w') in incompressible flows (Pope 2001). Poisson's equation links fluctuating velocities with pressure fluctuations. By manipulating the governing equations, it can be expressed as

$$\nabla^2 p' = -\rho \left(2 \frac{\overline{\partial u_i}}{\partial x_j} \frac{\partial u'_j}{\partial x_i} + \frac{\partial^2}{\partial x_i \partial x_j} \left(u'_i u'_j - \overline{u'_i u'_j} \right) \right), \tag{3.1}$$

where ∇^2 denotes the Laplacian operator, $\overline{u_i}$ represents the mean flow velocity and u'_i the fluctuating velocity components. The first term captures turbulence–mean-shear interaction (TMI), showing the impact of rapid mean flow variations induced by fluctuating flow. The second term represents turbulence–turbulence interaction (TTI), highlighting nonlinear interactions among turbulent structures. These terms are the main contributors to pressure fluctuations in the flow (Ma *et al.* 2023). Understanding interactions between the mean flow and turbulence, as well as among turbulent structures, is essential for analysing flow irregularity and destabilising mechanisms in the leading-edge shear layer. A similar approach was employed by Goswami & Hemmati (2024) and Goswami & Hemmati (2025) to analyse the flow dynamics and interactions in the wake.

Figure 21 illustrates the trends of TMI and TTI along the recirculating region. Along the leading-edge shear layer, TMI in figure 21(*a*) shows two prominent peaks of equal magnitude, corresponding to the onset of KHI and the primary vortex core. Since TMI represents the energy influx through mean flow modulation, the first peak at the onset of KHI indicates that energy is injected into the flow by mean flow modulation due to

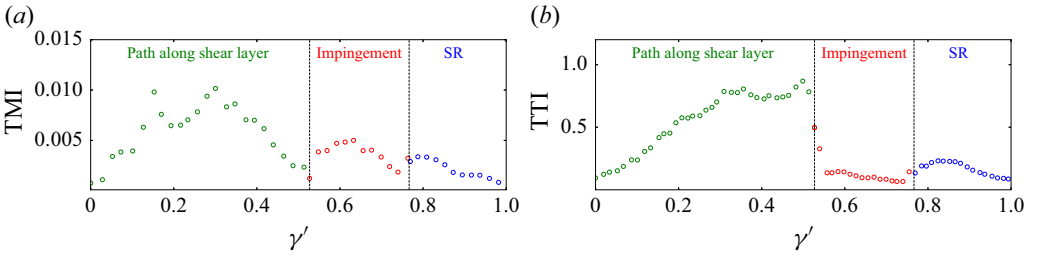

Figure 21. Trends of (*a*) turbulence–mean-shear interaction (TMI) and (*b*) turbulence–turbulence interaction (TTI) along the recirculating region. γ' represents the normalised curvilinear coordinate length.

the instability (Goswami & Hemmati 2024). The second peak at the primary vortex core signifies that energy is injected into the flow by amplified streamwise and normal velocity fluctuations (evident from figure 20*b*). Vorticity associated with the shear layer alters the mean flow in this region, resulting in enhanced momentum transport. Beyond this, TMI decreases towards the shear layer reattachment point, suggesting energy dissipation through flow reattachment (Mansour, Kim & Moin 1988). In the impingement region, TMI exhibits another peak, mainly due to spanwise sweeping of flow structures and heightened spanwise velocity fluctuations (Kumahor & Tachie 2023). Moving upstream into the SR, TMI shows a local maximum near the secondary vortex core, then decreases towards the leading edge, hinting at the mean flow modulation by the secondary vortex core and consequent energy influx into the flow. The TTI, shown in figure 21(*b*), increases steadily along the leading-edge shear layer, indicating strong interactions of leading-edge shear layer with downstream turbulent fluctuations. A peak near the primary vortex core suggests that these interactions are most intense downstream of the core. TTI then rises again until the reattachment location, where it sharply drops in the impingement region (symbols in red). This sharp drop, due to the upstream-moving reverse boundary layer, reflects reduced fluctuations along the reverse boundary layer (evident from figure 20*b*). Finally, TTI rises again near the secondary vortex core into the SR region, indicating that turbulence–turbulence interactions contribute energy to the leading-edge shear layer through mean flow modulation near the secondary vortex core, consistent with TMI trends (see figure 21*a*).

To analyse energy transfer along the recirculating region, figure 22 presents trends of turbulence kinetic energy production (P_k), dissipation (ε_k) and convection (C_k) along this region. Turbulence kinetic energy production is defined as $P_k = -(\overline{u_i' u_j'} - 2\overline{\nu_\tau S_{ij}})(\partial \overline{u_i}/\partial x_j)$, dissipation is defined as $\varepsilon_k = 2\overline{\tau_{ij}^{SGS} S_{ij}} + 2\nu \overline{S_{ij} S_{ij}}$ and convection is defined as $C_k = (1/2)(\overline{u_i})(\partial \overline{u_i' u_j'}/\partial x_i)$ (Pope 2001). As anticipated, P_k rises along the leading-edge shear layer, reaching a maximum at the point of peak streamwise velocity fluctuations (see figure 20*b*). Following this peak, P_k experiences a sharp drop and then exhibits steady production along the impingement region, consistent with expected trends from velocity fluctuations and mean shear stress. In the impingement region, mean shear stress ($\partial \overline{u}/\partial y$) decreases while streamwise and spanwise velocity fluctuations remain relatively constant, resulting in lower P_k. Further, profiles of ε_k suggest that energy is dissipated through flow impingement and the reverse boundary layer. Chiarini & Quadrio (2021) made similar observations, where large values of dissipation occurs in the core of PR. Intuitively, amplified dissipation in the reverse boundary layer confirms the larger degree of universality for the dissipative phenomena near a wall (Mansour *et al.* 1988). A peak of P_k is observed in SR, which is consistent with the

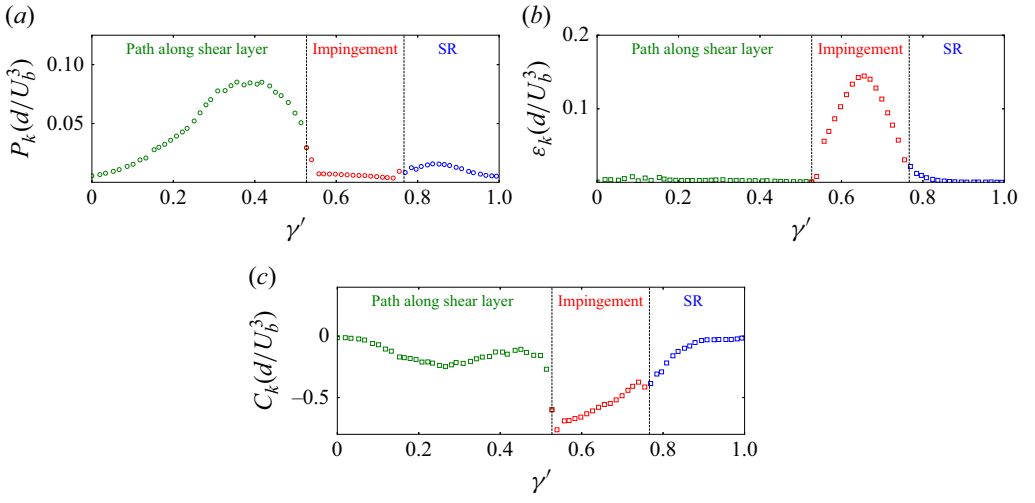

Figure 22. Trends of (*a*) turbulence kinetic energy production (P_k), (*b*) turbulent dissipation (ε_k) and (*c*) convection (C_k) along the recirculating region. γ' represents the normalised curvilinear coordinate length. Quantities are normalised by the free stream velocity and prism width.

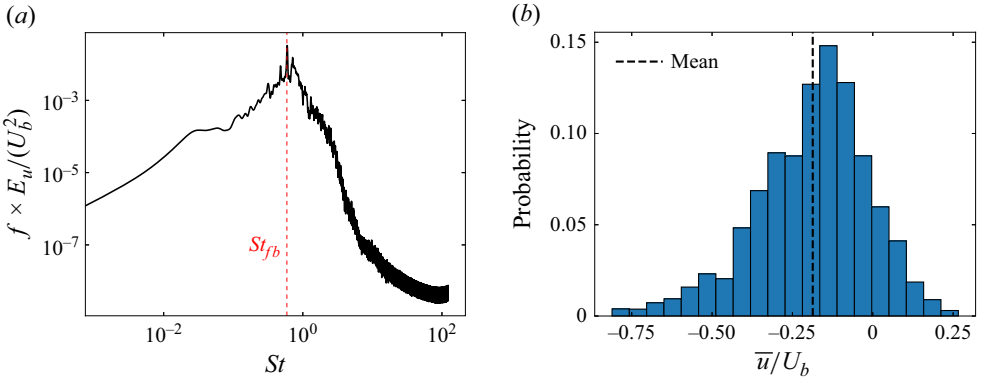

Figure 23. (*a*) Pre-multiplied power spectral density of streamwise velocity fluctuations (E_u) in SR, at $(x, y, z) = (0.5d, 1.05d, 0)$, and (*b*) probability density function of mean streamwise velocity ($\overline{u}$) along the secondary recirculation region.

amplified turbulence–turbulence interactions and velocity fluctuations. This indicates that energy is produced within SR. The convection profile (C_k) along SR shows a steady increase, suggesting that energy is transported upstream. Given the adverse pressure gradient and amplified convection in SR, turbulent fluctuations are able to reach the leading-edge shear layer, thus completing the cycle. This feedback mechanism establishes a continuous loop where flow structures generated in the SR region, through upstream convection and feedback at St_{fb}, influence the onset of the PR region. Notably, the steady spanwise and normal velocity fluctuations observed at the end of SR (figure 20*b*) are mirrored in the early part of PR, and the elevated TTI and P_k values near the secondary vortex core support this energetic linkage, confirming the physical proximity and dynamical similarity between these regions.

Figure 23(*a*) shows the pre-multiplied power spectral density of streamwise velocity fluctuations (E_u) along the SR, in the detached reverse flow region at $(0.5d, 1.05d, 0)$.

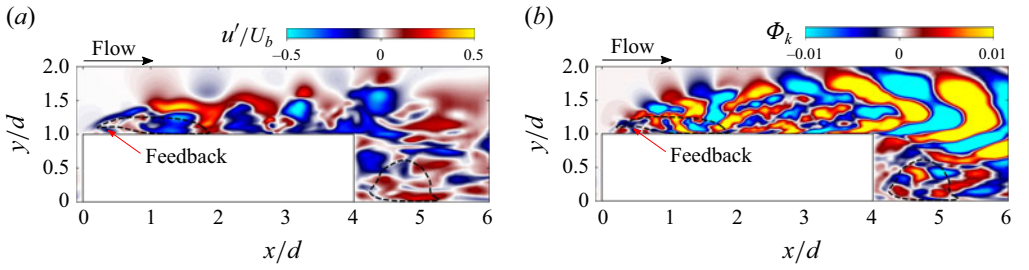

Figure 24. (*a*) Streamwise velocity fluctuation (u') showing feedback near the SR region; and (*b*) contours of the real part of the DMD mode for streamwise component corresponding to feedback frequency (St_{fb}), for the $DR = 4$ prism at $Re = 2.5 \times 10^3$.

Figure 23(*a*) indicates a distinct frequency corresponding to the feedback frequency (St_{fb}) observed earlier. A higher frequency peak is evident at St_{kh} and sub-harmonics of St_{fb} are noted; however, the peak in the premultiplied frequency spectrum at $St_{fb} \approx 0.59$ is most prominent. The probability density function of the mean streamwise velocity along the SR region (figure 23*b*) reveals strong upstream advection characterised by a negative mean streamwise velocity. This finding further supports the upstream convection of energy by flow structures at the feedback frequency along the SR region. The long negative tail of the probability density function suggests rare but strong reverse flow events in this region, which are associated with the upstream transfer of energy generated in the SR. Since St_{fb} is much lower than the frequency of KHI, flow structures in the SR tend to cluster and amplify, as evidenced by the high probability of near-zero mean streamwise velocity. These clusters then move upstream towards the leading edge, contributing to the destabilisation of the leading-edge shear layer. A vortex reconnection phenomenon is also anticipated (Cimarelli *et al.* 2018), where streamwise vortices stretch in the spanwise direction due to the feedback effect. This is consistent with the stronger spanwise velocity fluctuations along the SR (figure 20*b*) and the lower streamwise fluctuations. Finally, figure 24(*a*) shows contours of streamwise velocity fluctuations (u'), revealing feedback effects near the SR. Here, a region of negative streamwise velocity fluctuations is evident in the SR. The DMD mode corresponding to St_{fb} is presented in figure 24(*b*), illustrating streamwise vortices that signal feedback from the SR into the leading-edge shear layer.

3.4.2. *Streamline following free shear layer*

The critical streamline representing the path following free shear layer is shown in figure 25. Similar to the recirculating region, the path following free shear layer is divided into three sub-regions: (i) the area following the leading-edge shear layer up to the flow reattachment on the prism surface (highlighted in green); (ii) the flow along the attached boundary layer (in red); and (iii) flow development in the wake of $DR = 4$. Similar to the recirculating region, analysing the path following free shear layer provides insights into the first branch of turbulent flow structures emerging from the leading-edge shear layer and moving downstream into the wake.

Evolution of pressure and root-mean-squared velocity fluctuations (u'_{rms}, v'_{rms}, w'_{rms}) along the path following free shear layer are shown in figure 26. Mean pressure along the shear-layer path (shown in green) aligns with the corresponding section in the recirculating region. Initially, pressure decreases up to the location of the primary vortex core, then increases due to the adverse pressure gradient until shear-layer reattachment on the prism surface. This adverse gradient is sustained in the attached boundary-layer region (shown in red), followed by a slight reduction due to a favourable pressure gradient extending

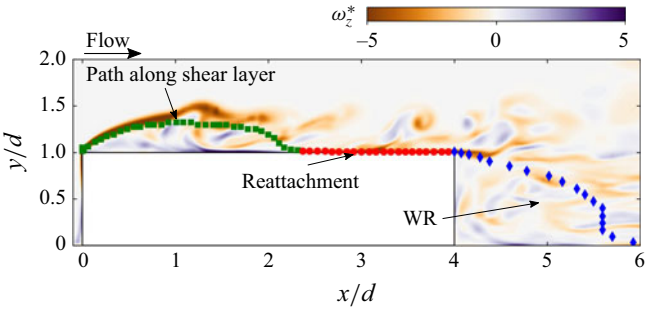

Figure 25. Contours of spanwise vorticity (ω_z^*) overlapped with critical streamline representing the path following free shear layer, at $Re = 2.5 \times 10^3$ for the $DR = 4$ prism.

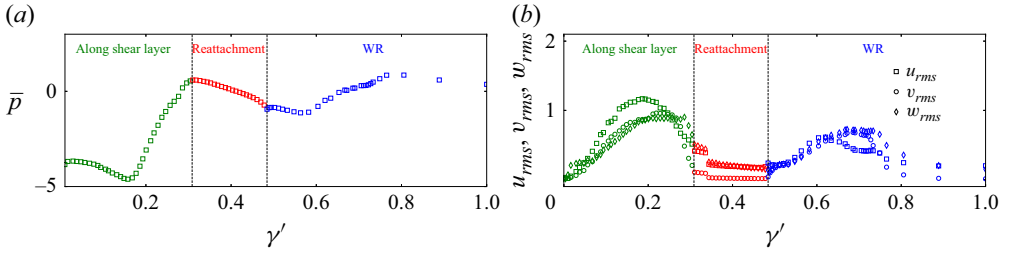

Figure 26. Trends of (*a*) pressure and (*b*) root-mean-squared velocity fluctuations (u'_{rms}, v'_{rms}, w'_{rms}) along the path following free shear layer for the $DR = 4$ prism at $Re = 2.5 \times 10^3$. γ' represents the normalised curvilinear coordinate length.

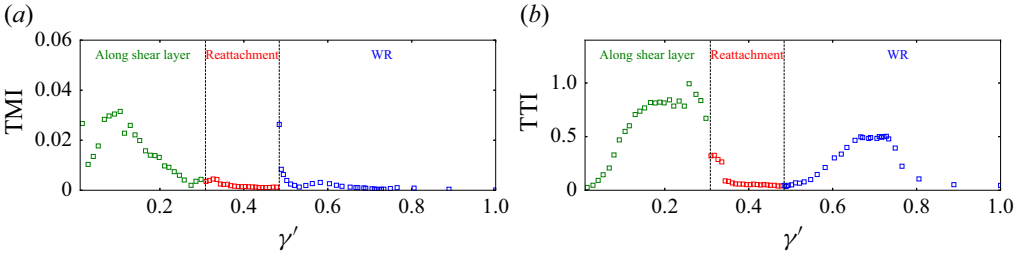

Figure 27. Trends of (*a*) turbulence–mean-shear interaction (TMI) and (*b*) turbulence–turbulence interaction (TTI) along the path following free shear layer. γ' represents the normalised curvilinear coordinate length.

to the trailing edge. This favourable gradient continues into the WR (blue), where it reaches a local minimum before returning to its free stream value downstream. Turbulence intensities in figure 26(*b*) increase along the leading-edge shear layer, following trends observed in the recirculating region. Instabilities amplify in this region, leading to shear-layer roll-up and the formation of spanwise vortex structures. Near the reattachment point, turbulence intensities drop sharply until normal velocity fluctuations become negligible in the attached boundary layer. As the boundary layer develops downstream and detaches at the trailing edge, turbulence intensities increase. In WR, turbulence fluctuations grow further due to mixing and interactions between spanwise and normal flow structures in the recirculating flow.

To further examine mean flow modulation and turbulent flow interactions, TMI and TTI along the path following free shear layer are shown in figure 27. As anticipated, TMI

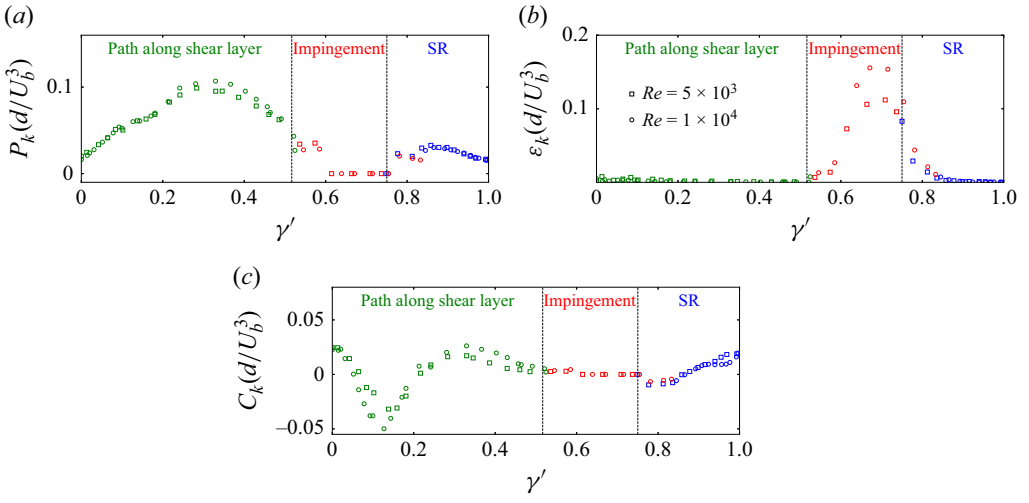

Figure 28. Trends of (*a*) turbulence kinetic energy production (P_k), (*b*) turbulent dissipation (ε_k) and (*c*) convection (C_k) along the recirculating region for (□) $Re = 5 \times 10^3$ and (○) 1×10^4. γ' represents the normalised curvilinear coordinate length. P_k and C_k are normalised by the free stream velocity and prism width.

increases to its maximum near the secondary vortex core. Since the SR convects energy upstream into the leading-edge shear layer, mean flow modulation occurs closer to the leading edge, as indicated by the TMI peak. Following this peak, TMI drops sharply as the flow reattaches to the prism surface. Due to the negligible velocity fluctuations in the attached boundary-layer region (shown in red), mean flow modulation is also minimal until the flow separates again at the trailing edge. A local maximum is observed right at the trailing-edge separation point, decreasing significantly into the WR and downstream. WR is primarily characterised by spanwise and normal flow variations (Kumahor & Tachie 2023), which is evident from the profiles in figure 26(*b*). Thus, mean flow modulation is minimal here, as turbulence intensities are largely driven by the mixing of spanwise and normal flow structures (Chiarini & Quadrio 2021). As expected, TTI (in figure 27*b*) rises along the shear layer, reaches its peak and then decreases again upon flow reattachment to the prism surface. Turbulent interactions are minimal along the attached boundary layer and increase again in the WR. Due to the mixing and interaction of flow structures along WR, turbulence–turbulence interactions intensify, promoting the growth of turbulence intensities in this area. While the feedback mechanism shares similarities with the destabilisation process reported by Cimarelli *et al.* (2018), our analysis provides insights into the development of turbulent flow structures in the recirculating region as well as the path of energy transport, which leads to the growth of turbulence intensities and shear-layer destabilisation.

3.5. *High-Reynolds-number flow*

The destabilisation mechanism described here persists at higher Reynolds numbers, which is apparent from the results at $Re = 5 \times 10^3$ and $Re = 1 \times 10^4$. Figure 28 shows the trends of P_k and C_k along the recirculating region at $Re = 5 \times 10^3$ and $Re = 1 \times 10^4$, which align with those observed at $Re = 2.5 \times 10^3$. Specifically, P_k is most pronounced along the leading-edge shear layer and sharply decreases after the shear-layer reattachment, where energy dissipates (evident from figure 28*b*) and turbulence intensities drop notably in the impingement region. Additionally, P_k exhibits a secondary peak near the location of

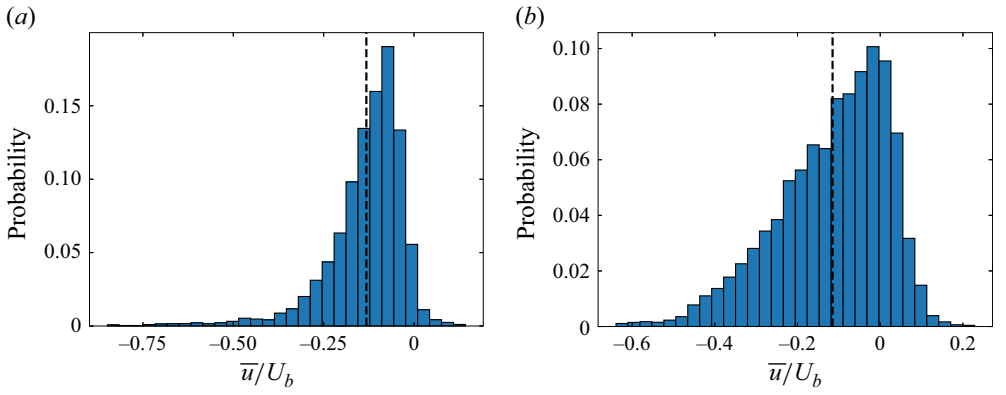

Figure 29. Probability density function of mean streamwise velocity ($\overline{u}$) along the secondary recirculation region for (*a*) $Re = 5 \times 10^3$ and (*b*) 1×10^4. Dashed line represents the mean streamwise velocity.

the secondary vortex core, signifying energy production by the secondary recirculation region. The energy convection trends match the production patterns, showing that energy is carried upstream by flow structures. The probability density function of mean streamwise velocity ($\overline{u}$) in the SR for $Re = 5 \times 10^3$ and $Re = 1 \times 10^4$ is presented in figure 29. These trends are consistent with those observed at $Re = 2.5 \times 10^3$, indicating rare yet intense upstream convection events of flow structures. Such events amplify energy within the SR region, and are expected to cluster and propagate upstream towards the leading edge, contributing to destabilisation of the leading-edge shear layer.

4. Conclusion

The destabilisation mechanism of the leading-edge shear layer and the onset of Kelvin–Helmholtz instability were evaluated at high Reynolds numbers ($Re = 2.5 \times 10^3$, 5×10^3 and 1×10^4) for the cases of $AR = 0.25-1.5$ and $DR = 1-4$. Wake unsteadiness enhanced with increasing depth ratio and KHI was noted for all cases, forming finite spanwise vortex rollers. Moreover, depth ratio influenced the intensity of mean shear stress experienced by the downstream flow, significantly impacting the inception and evolution of hairpin-like vortices in the wake. The onset of KHI closer to the leading-edge for long prisms ($DR \geqslant 3$) resulted in the shear-layer roll-up and spanwise elongated vortex structures appearing on the prism surfaces. At higher Reynolds numbers, the onset of KHI shifted upstream and closer to the leading-edge, maximising turbulence kinetic energy and the accumulation of energy, leading to enhanced flow irregularity for long prisms. Furthermore, destabilisation of the leading-edge shear layer was investigated quantitatively by focusing on the recirculating region and the path following the free shear layer. Results highlighted the crucial role of secondary recirculation regions in modulating flow structures and facilitated upstream convection of energy, which in turn destabilised the leading-edge shear layer. Flow structures in SR were clustered due to vortex reconnection, and thus amplified. A feedback mechanism was noted, where the clustered and energised structures moved upstream towards the leading edge, transferring energy into the leading-edge shear layer and resulting in its destabilisation. Turbulence kinetic energy production and convection distributions revealed that the destabilisation process was closely related to energy production in both primary and secondary recirculation zones. Here, energy was produced by the secondary recirculation and convected upstream, driving further instability. Probability density functions revealed the presence of rare and intense upstream

convection events, which amplified turbulence and facilitated the destabilisation process, regardless of Reynolds number. Thus, this study quantified the impact of secondary vortex interactions, feedback mechanism and vortex reconnection phenomena in enhancing turbulence intensities, which ultimately led to the shear-layer destabilisation and flow separation.

Acknowledgments. This research has received support from the Natural Sciences and Engineering Research Council of Canada (NSERC) and Alberta Innovates. The computational analysis was completed using Digital Research Alliance of Canada computing clusters.

Declaration of interests. The authors report no conflict of interests.

References

BECKER, S., LIENHART, H. & DURST, F. 2002 Flow around three-dimensional obstacles in boundary layers. *J. Wind Engng Ind. Aerodyn.* **90** (4-5), 265–279.

BEHERA, S. & SAHA, A.K. 2019 Characteristics of the flow past a wall-mounted finite-length square cylinder at low Reynolds number with varying boundary layer thickness. *J. Fluids Engng* **141** (6), 061204.

BOURGEOIS, J.A., SATTARI, P. & MARTINUZZI, R.J. 2011 Alternating half-loop shedding in the turbulent wake of a finite surface-mounted square cylinder with a thin boundary layer. *Phys. Fluids* **23** (9), 095101.

CAO, Y., TAMURA, T., ZHOU, D., BAO, Y. & HAN, Z. 2022 Topological description of near-wall flows around a surface-mounted square cylinder at high Reynolds numbers. *J. Fluid Mech.* **933**, A39.

CELIK, I., KLEIN, M. & JANICKA, J. 2009 Assessment measures for engineering LES applications. *ASME. J. Fluids Engng* **131** (3), 031102.

CHIARINI, A. & QUADRIO, M. 2021 The turbulent flow over the BARC rectangular cylinder: a DNS study. *Flow Turbul. Combust.* **107**, 875–899.

CIMARELLI, A., CORSINI, R. & STALIO, E. 2024 Reynolds number effects in separating and reattaching flows with passive scalar transport. *J. Fluid Mech.* **984**, A20.

CIMARELLI, A., LEONFORTE, A. & ANGELI, D. 2018 On the structure of the self-sustaining cycle in separating and reattaching flows. *J. Fluid Mech.* **857**, 907–936.

DUONG, D.V., VAN NGUYEN, L., VAN NGUYEN, D., DINH, T.C., ZUHAL, L.R. & NGO, L.I. 2024 Direct numerical simulation of 45° oblique flow past surface-mounted square cylinder. *J. Fluid Mech.* **992**, A12.

DURBIN, P.A. & REIF, B.A.P. 2011 *Statistical Theory and Modeling for Turbulent Flows*. John Wiley & Sons.

EL HASSAN, M., BOURGEOIS, J. & MARTINUZZI, R. 2015 Boundary layer effect on the vortex shedding of wall-mounted rectangular cylinder. *Exp. Fluids* **56** (2), 1–19.

GOSWAMI, S. 2025 Wake transitions and interactions behind wall-mounted prisms. PhD thesis, University of Alberta.

GOSWAMI, S. & HEMMATI, A. 2020 Response of turbulent pipeflow to multiple square bar roughness elements at high Reynolds number. *Phys. Fluids* **32** (7), 075110.

GOSWAMI, S. & HEMMATI, A. 2021*a* Evolution of turbulent pipe flow recovery over a square bar roughness element at a range of Reynolds numbers. *Phys. Fluids* **33** (3), 035113.

GOSWAMI, S. & HEMMATI, A. 2021*b* Response of viscoelastic turbulent pipeflow past square bar roughness: the effect on mean flow. *Computation* **9** (8), 85.

GOSWAMI, S. & HEMMATI, A. 2022 Mechanisms of wake asymmetry and secondary structures behind low aspect-ratio wall-mounted prisms. *J. Fluid Mech.* **950**, A31.

GOSWAMI, S. & HEMMATI, A. 2023 Mean wake evolution behind low aspect-ratio wall-mounted finite prisms. *Intl J. Heat Fluid Flow* **104**, 109237.

GOSWAMI, S. & HEMMATI, A. 2024 Impact of depth-ratio on shear-layer dynamics and wake interactions around wall-mounted prisms. *Phys. Fluids* **36** (11), 115149.

GOSWAMI, S. & HEMMATI, A. 2025 Influence of depth-ratio on turbulence transition in the wake of wall-mounted prisms. *J. Fluid Mech.* **1007**, A9.

HOSSEINI, Z., BOURGEOIS, J.A. & MARTINUZZI, R.J. 2013 Large-scale structures in dipole and quadrupole wakes of a wall-mounted finite rectangular cylinder. *Exp. Fluids* **54** (9), 1–16.

HUSSEIN, H.J. & MARTINUZZI, R.J. 1996 Energy balance for turbulent flow around a surface mounted cube placed in a channel. *Phys. Fluids* **8** (3), 764–780.

HWANG, J.-Y. & YANG, K.-S. 2004 Numerical study of vortical structures around a wall-mounted cubic obstacle in channel flow. *Phys. Fluids* **16** (7), 2382–2394.

JIA, Y., PUNITHAKUMAR, K., NOGA, M. & HEMMATI, A. 2021 Blood flow manipulation in the aorta with coarctation and arch narrowing for pediatric subjects. *J. Appl. Mech.* **88** (2), 021001.

JIANG, G. & YOSHIE, R. 2020 Side ratio effects on flow and pollutant dispersion around an isolated high-rise building in a turbulent boundary layer. *Build. Environ.* **180**, 107078.
JIMENEZ, J. 1983 A spanwise structure in the plane shear layer. *J. Fluid Mech.* **132**, 319–336.
KHALID, M.S.U., WANG, J., AKHTAR, I., DONG, H. & LIU, M. 2020 Modal decompositions of the kinematics of Crevalle jack and the fluid–caudal fin interaction. *Bioinspir. Biomim.* **16** (1), 016018.
KINDREE, M.G., SHAHROODI, M. & MARTINUZZI, R.J. 2018 Low-frequency dynamics in the turbulent wake of cantilevered square and circular cylinders protruding a thin laminar boundary layer. *Exp. Fluids* **59** (12), 1–26.
KIYA, M. & SASAKI, K. 1983 Structure of a turbulent separation bubble. *J. Fluid Mech.* **137**, 83–113.
KUMAHOR, S. & TACHIE, M.F. 2022 Turbulent flow around rectangular cylinders with different streamwise aspect ratios. *J. Fluids Engng* **144** (5), 051304.
KUMAHOR, S. & TACHIE, M.F. 2023 Effects of streamwise aspect ratio on the spatio-temporal characteristics of flow around rectangular cylinders. *Intl J. Heat Fluid Flow* **101**, 109133.
LI, Y., ZHANG, J., DONG, G. & ABDULLAH, N.S. 2020 Small-scale reconstruction in three-dimensional kolmogorov flows using four-dimensional variational data assimilation. *J. Fluid Mech.* **885**, A9.
MA, C.-H., AWASTHI, M., MOREAU, D. & DOOLAN, C. 2023 Aeroacoustics of turbulent flow over a forward–backward facing step. *J. Sound Vib.* **563**, 117840.
MANGRULKAR, C.K., DHOBLE, A.S., CHAKRABARTY, S.G. & WANKHEDE, U.S. 2017 Experimental and CFD prediction of heat transfer and friction factor characteristics in cross flow tube bank with integral splitter plate. *Intl J. Heat Mass Transfer* **104**, 964–978.
MANSOUR, N.N., KIM, J. & MOIN, P. 1988 Reynolds-stress and dissipation-rate budgets in a turbulent channel flow. *J. Fluid Mech.* **194**, 15–44.
MARTINUZZI, R. & TROPEA, C. 1993 The flow around surface-mounted, prismatic obstacles placed in a fully developed channel flow (data bank contribution). *J. Fluids Eng.* **115** (1), 85–92.
MOIN, P. & MAHESH, K. 1998 Direct numerical simulation: a tool in turbulence research. *Annu. Rev. Fluid Mech.* **30** (1), 539–578.
MOORE, D.M., LETCHFORD, C.W. & AMITAY, M. 2019*a* Energetic scales in a bluff body shear layer. *J. Fluid Mech.* **875**, 543–575.
MOORE, D.M., LETCHFORD, C.W. & AMITAY, M. 2019*b* Transitional shear layers on rectangular sections. In Proceedings of the XV Conference of the Italian Association for Wind Engineering: IN-VENTO 2018, vol. 25, pp. 519–533. Springer.
PAUL, J.C., JOHNSON, R.W. & YATES, R.G. 2009 Application of CFD to rail car and locomotive aerodynamics. In *The Aerodynamics of Heavy Vehicles II: Trucks, Buses, and Trains* (ed. J.C. Paul, R.W. Johnson & R.G. Yates), pp. 259–297. Springer.
POPE, S.B. 2001 Turbulent flows. *Meas. Sci. Technol.* **12** (11), 2020–2021.
RASTAN, M.R., SHAHBAZI, H., SOHANKAR, A., ALAM, M.M. & ZHOU, Y. 2021 The wake of a wall-mounted rectangular cylinder: cross-sectional aspect ratio effect. *J. Wind Engng Ind. Aerodyn.* **213**, 104615.
RASTAN, M.R., SOHANKAR, A. & ALAM, M.M. 2017 Low-Reynolds-number flow around a wall-mounted square cylinder: flow structures and onset of vortex shedding. *Phys. Fluids* **29** (10), 103601.
SAEEDI, M., LEPOUDRE, P.P. & WANG, B.-C. 2014 Direct numerical simulation of turbulent wake behind a surface-mounted square cylinder. *J. Fluids Struct.* **51**, 20–39.
SAHA, A.K. 2013 Unsteady flow past a finite square cylinder mounted on a wall at low Reynolds number. *Comput. Fluids* **88**, 599–615.
SAKAMOTO, H. & ARIE, M. 1983 Vortex shedding from a rectangular prism and a circular cylinder placed vertically in a turbulent boundary layer. *J. Fluid Mech.* **126**, 147–165.
SHOJAEE, S.A., GOSWAMI, S., LANGE, C.F. & HEMMATI, A. 2025 A neural network approach to improve Reynolds-averaged Navier–Stokes modeling of bluff body wakes. *AIP Adv.* **15** (2), 025018.
SIGURDSON, L.W. 1995 The structure and control of a turbulent reattaching flow. *J. Fluid Mech.* **298**, 139–165.
SMITS, A., DING, L. & VAN BUREN, T. 2019 Flow over a square bar roughness. In *Proceedings of Turbulence and Shear Flow Phenomena*, vol. 11. TSFP11.
SOHANKAR, A., NORBERG, C. & DAVIDSON, L. 1998 Low-Reynolds-number flow around a square cylinder at incidence: study of blockage, onset of vortex shedding and outlet boundary condition. *Intl J. Numer. Meth. Fluids* **26** (1), 39–56.
TAIRA, K., HEMATI, M.S., BRUNTON, S.L., SUN, Y., DURAISAMY, K., BAGHERI, S., DAWSON, S.T.M. & YEH, C.-A. 2020 Modal analysis of fluid flows: applications and outlook. *AIAA J.* **58** (3), 998–1022.
TOMINAGA, Y. 2015 Flow around a high-rise building using steady and unsteady RANS CFD: effect of large-scale fluctuations on the velocity statistics. *J. Wind Engng Ind. Aerodyn.* **142**, 93–103.

UFFINGER, T., ALI, I. & BECKER, S. 2013 Experimental and numerical investigations of the flow around three different wall-mounted cylinder geometries of finite length. *J. Wind Engng Ind. Aerodyn.* **119**, 13–27.
VON KÁRMÁN, T. 1963 *Aerodynamics*. vol. 9. McGraw-Hill New York.
WANG, F. & LAM, K.M. 2019 Geometry effects on mean wake topology and large-scale coherent structures of wall-mounted prisms. *Phys. Fluids* **31** (12), 125109.
WANG, H.F. & ZHOU, Y. 2009 The finite-length square cylinder near wake. *J. Fluid Mech.* **638**, 453–490.
WANG, H.F., ZHOU, YU, CHAN, C.K. & LAM, K.S. 2006 Effect of initial conditions on interaction between a boundary layer and a wall-mounted finite-length-cylinder wake. *Phys. Fluids* **18** (6), 065106.
YAKHOT, A., LIU, H. & NIKITIN, N. 2006 Turbulent flow around a wall-mounted cube: a direct numerical simulation. *Intl J. Heat Fluid Flow* **27** (6), 994–1009.
YAUWENAS, Y., PORTEOUS, R., MOREAU, D.J. & DOOLAN, C.J. 2019 The effect of aspect ratio on the wake structure of finite wall-mounted square cylinders. *J. Fluid Mech.* **875**, 929–960.
ZARGAR, A., TAROKH, A. & HEMMATI, A. 2022 The unsteady wake transition behind a wall-mounted large-depth-ratio prism. *J. Fluid Mech.* **952**, A12.
ZHANG, D., CHENG, L., AN, H. & ZHAO, M. 2017 Direct numerical simulation of flow around a surface-mounted finite square cylinder at low Reynolds numbers. *Phys. Fluids* **29** (4), 045101.
ZHANG, Z., KAREEM, A., XU, F. & JIANG, H. 2023 Global instability and mode selection in flow fields around rectangular prisms. *J. Fluid Mech.* **955**, A19.
ZHENG, H., XIE, F., ZHENG, Y., JI, T. & ZHU, Z. 2019 Propulsion performance of a two-dimensional flapping airfoil with wake map and dynamic mode decomposition analysis. *Phys. Rev. E* **99** (6), 063109.